THE JOURNAL OF PHYSICAL CHEMISTRY C
A JOURNAL OF THE AMERICAN CHEMICAL SOCIETY

pubs.acs.org/JPCC

Article

Electronic and Thermoelectric Properties of Transition-Metal Dichalcogenides

Daniel I. Bilc,* Diana Benea, Viorel Pop, Philippe Ghosez, and Matthieu J. Verstraete

Cite This: https://doi.org/10.1021/acs.jpcc.1c07088

Read Online

ACCESS | Metrics & More | Article Recommendations | Supporting Information

ABSTRACT: Using first-principles electronic structure calculations performed within the B1-WC hybrid functional, we study the thickness and strain dependency of electronic and thermoelectric (TE) properties of transition-metal dichalcogenides (TMDs). We consider both 2H (MoS_2, $MoSe_2$, $MoTe_2$, WS_2, WSe_2, WTe_2) and 1T (SnS_2, $SnSe_2$, HfS_2, $HfSe_2$, $HfTe_2$, ZrS_2, $ZrSe_2$) structures and identify those TMDs with a high TE potential (WSe_2, $MoTe_2$, and $SnSe_2$). The thickness and strain significantly change the electronic properties near the forbidden band gaps. We rationalize at an atomic level these changes in terms of the interplay between in-plane bonding/antibonding X−X(M−M) interactions through sp^2 hybridization and the stronger antibonding/nonbonding M−X interactions due to sp^3d and sp^3d^2 hybridizations inside TMD layers (X, chalcogen; M, transition metal, Sn). Thickness and in-plane strain appear as effective ways to tune electronic band structures, increase the degeneracy of carrier pockets, and optimize the TE properties of TMDs. We estimate the anisopropy of carrier pockets and introduce the effective mass quality factor B_m for the maximization of TE performance at a given carrier density and temperature. High-potential TMDs have B_m and power factors comparable to PbTe and Bi_2Te_3.

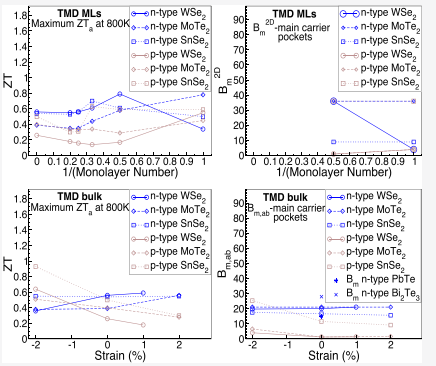

1. INTRODUCTION

Transition-metal dichalcogenides (TMDs), having the chemical formula MX_2 (M = Mo, W, Hf, Zr, Sn, and X = S, Se, Te), are two-dimensional (2D) materials consisting of XMX atomic layers with strong chemical bonds inside the layers and weak van der Waals (vdW)-type interactions between the layers. They offer huge flexibility in tuning electronic and transport properties since their electronic structure is found to change dramatically from a bulk to a single XMX layer (monolayer, ML).[1−3] TMDs possess high strength and can sustain strains of up to 10%,[4] allowing effective tuning of electronic properties also by strain. TMDs are emerging as next-generation semiconductor materials possessing unusual properties such as the lattice-symmetry-induced valley Hall effect,[5,6] the spin Hall effect,[7] valley polarization,[8−10] anomalous giant magnetoresistance,[11] and superconductivity.[12−17] In single MLs of TMDs, high carrier mobilities are expected at room temperature based on theoretical predictions.[18−20] TMDs exhibit novel topological electronic phases[21−23] being closely related to Bi_2Te_3 and Bi_2Se_3 layered thermoelectric (TE) materials, which were the first demonstrated topological semiconductors. There are specific advantages of 2D materials, both for specific applications (requiring low mass, flexibility, integration, etc.) and for their ease of assembly and emergent behavior of record high thermal insulation across ultrathin TMD heterostructures having a low effective thermal conductivity of 0.007−0.009 W/(m K) at 300 K.[24] The low-dimensional character of electronic transport,[25,26] high carrier mobilities along the transport direction,[27] carrier pocket degeneracy,[28] and highly anisotropic electronic bands active in transport[29,30] are key ingredients to maximize TE performance defined by the dimensionless figure of merit, $ZT = (S^2\sigma T)/\kappa_{th}$, where σ is the electrical conductivity, S is the thermopower or the Seebeck coefficient, T is the absolute temperature, κ_{th} is the total thermal conductivity including electronic and lattice contributions, and $S^2\sigma$ is the power factor (PF). Improving the TE efficiency is not obvious because the transport parameters entering ZT are interdependent. From these perspectives, TMDs are good candidates to decouple the interplay between transport parameters and improve the TE efficiency,[31] by exploiting their 2D nature and the effect of thickness and strain on electronic properties. TMDs have the most stable bulk structures formed under either 2H or 1T polymorphs. The 3R polymorphs have only been seen in few-monolayer-thick structures and remain a great challenge to achieve in bulk or thicker films of TMDs, with a larger lateral size, as is required for practical TE applications.[32]

Many first-principles studies of electronic properties of TMDs and their monolayers have been reported in the literature. TE properties were theoretically estimated for

Received: August 10, 2021
Revised: November 17, 2021

HfS_2,[33,34] $HfSe_2$,[33] ZrS_2,[33,34] $ZrSe_2$,[33] SnS_2,[35,36] $SnSe_2$,[36,37] MoS_2,[38] MoS_2 ML and WSe_2 ML,[39,40] MX_2 ML (M = Mo, W, Zr, Hf; X = S, Se, Te),[41,42] and HfS_2 ML[43] predicting high TE performance. The thickness dependence of electronic properties for SnS_2, $SnSe_2$,[44] MX_2 (M = Mo, W; X = S, Se),[45] and MoS_2[46] and the strain effect on the electronic band structure of TMD MLs[47−49] show the tunability of electronic band gaps with thickness and strain. In this work, the structural, electronic, and TE properties of TMDs with 2H ($MoSe_2$, WSe_2, MoS_2, WS_2, and $MoTe_2$) and 1T ($ZrSe_2$, $HfSe_2$, $SnSe_2$, ZrS_2, HfS_2, and SnS_2) structures were studied within the B1-WC[50] hybrid functional, which gives simultaneously good accuracy for their structural (a, c lattice parameters and c/a ratio) and electronic (band gap) properties. The thickness dependence for 1−5 monolayers (MLs) and for the first time the strain dependence for bulk TMDs were studied identifying their effect on the electronic and TE properties. The electronic properties (band structures) of TMDs were found to be strongly dependent on the layer thickness and the applied epitaxial strain and more specifically on the ability of exchange−correlation functionals to describe c/a structural ratios. The epitaxial strain can be used to increase the energy degeneracy of carrier pockets in the conduction and valence bands to optimize TE properties. We also analyzed the anisotropy of carrier pockets and introduced a new effective mass quality factor B_m, which maximizes TE performance (ZT) at a given carrier concentration n and T. B_m is directly proportional to the TE quality factor B that maximizes ZT for very large B values.

2. TECHNICAL DETAILS

The structural, electronic, and TE properties of TMD structures are studied within the density functional theory (DFT) formalism using the B1-WC hybrid functional.[50] B1-WC describes the electronic (band gaps) and structural properties with better accuracy than the usual simple functionals and is more appropriate for correlated materials with d electronic states.[50−52] The electronic structure calculations were performed using the linear combination of the atomic orbitals method as implemented in the CRYSTAL code.[53] We used localized Gaussian-type basis sets including polarization orbitals and considered all of the electrons for Zr,[54] S,[55] and Se.[56] Hartree−Fock pseudopotentials for Mo,[57] W,[60] Hf,[61] Sn,[57] and Te[57] were used. The exponents of the most diffuse valence and polarization Gaussian functions were optimized in B1-WC to minimize the total energy of bulk TMDs (Supporting Information). It is known that the spin−orbit interaction (SOI) is important for the optical properties of TMDs but not for structural or vibrational[58] ones. We have checked the effect of SOI on the TE properties for the monolayer and bulk structures of WSe_2 and $SnSe_2$ within the B1-WC partial hybrid implementation of the WIEN2K[59] code: TE properties (PF) are not significantly affected by SOI at optimal doping (Supporting Information).

Brillouin zone integration is performed using the following meshes of k-points: 6 × 6 × 6 for bulk TMDs and 6 × 6 × 1 for 1−5 MLs of TMDs. The self-consistent-field calculations were considered to be converged when the energy changes between interactions were smaller than 10^{-8} hartree. An extralarge predefined and pruned grid consisting of 75 radial points and 974 angular points was used for the numerical integration of the charge density. Full optimizations of the lattice constants and atomic positions were performed with the optimization convergence of 5 × 10^{-5} hartree/bohr in the root-mean-square values of forces and 1.2 × 10^{-3} bohr in the root-mean-square values of atomic displacements. The level of accuracy in evaluating the Coulomb and exchange series is controlled by five tolerance parameters (10^{-ITOL_j}, j = 1−5).[53] The ITOL values used in our calculations are 7, 7, 7, 9, and 30.

The transport properties are calculated within the Boltzmann transport formalism and the constant relaxation time approximation using the BoltzTraP transport code.[62] Other approaches have been used in the literature, within the Boltzmann approximation, but with an ab initio relaxation time based on phonon or impurity scattering, e.g., refs 20 and 63−65. These show interesting effects but are much heavier to calculate: our goal is to be systematic and compare the different TMDs on the same footing. We estimate experimental relaxation times and include a generic $1/T$ temperature dependence for the acoustic and optical phonon scatterings at high T. The transport coefficients were very well converged for the energies calculated on k-point meshes of 67 × 67 × 37 for TMDs with a 2H structure, 47 × 47 × 41 for TMDs with a 1T structure, and 167 × 167 × 1 for 1−5 MLs of TMDs (non-self-consistent calculations of the DFT eigen energies).

The effective masses were obtained by calculating energies close to the conduction band (CB) minimum and valence band (VB) maximum while moving from the extremum points along the three directions of the orthogonal reciprocal lattice vectors k_i (i = x, y, z). The energy values, $\epsilon_{\vec{k}}$, were expanded about the extremum points and fit up to 10th-order polynomials in k_i yielding

$$\frac{2m_e}{\hbar^2}\epsilon_{\vec{k}} = \sum_i \frac{m_e}{m_{ii}}k_i^2 + \cdots + O(k_i^{10}) \quad (1)$$

where m_{ii} are the components of the effective mass tensor (i = x, y, z) and m_e is the free electron mass.

3. RESULTS

3.1. Structural and Electronic Properties of Bulk TMDs. The structural and electronic properties of TMDs studied within B1-WC using optimized Gaussian basis sets are presented in Tables 1 and 2. The lattice parameters a and c and the c/a ratio within B1-WC are described with good accuracy (the largest deviation from the experiment is ∼4.5% for c and the c/a ratio of $ZrSe_2$ and SnS_2) and compare well with the values obtained within the PBE + D3/D2[66] functional, which includes D3/D2[67] dispersion corrections for van der Waals interactions (the largest deviation from the experiment is ∼0.9% for c and ∼1.8% for the c/a ratio of $HfSe_2$ and SnS_2). The indirect band gaps E_g obtained within B1-WC are in very good agreement with the experiment for TMDs with the 1T structure (except for $ZrSe_2$) and slightly overestimated by ∼0.2−0.3 eV for TMDs with the 2H structure. PBE + D3/D2 underestimates E_g values in some cases, up to ∼1−2 eV. The electronic properties of TMDs are better studied with hybrid functionals (PBE0,[68,69] B3LYP,[68] HSE[68,70,74,75]) or meta-generalized gradient approximations (meta-GGAs) like the modified Becke−Johnson potential[33,68] or the GW[71,72,75] and GVJ-2e[73] methods. All give good agreement with the experiment for E_g, whether at the experimental lattice parameters or using optimized values from PBE + D3/D2,[74,75] PBE0 + D3,[69] and vdW-TS[70] calculations. B1-WC gives a good agreement with the experiment simultaneously for

https://doi.org/10.1021/acs.jpcc.1c07088
J. Phys. Chem. C XXXX, XXX, XXX−XXX

Table 1. Lattice Parameters a and c, the c/a Ratio, and Indirect Band Gap E_g of TMDs with the 2H Structure (Space Group $P6_3/mmc$) Estimated within B1-WC[f]

		a (Å)	c (Å)	c/a	E_g (eV)
MoS_2	B1-WC	3.137	12.235	3.90	1.58
	PBE + D3	3.16	12.34	3.91	0.92
	exp	3.157	12.272	3.89	1.23−1.29[a]
WS_2	B1-WC	3.158	12.194	3.86	1.7
	PBE + D3	3.16	12.42	3.93	1.04
	exp	3.154	12.360	3.92	1.35−1.44[b]
$MoSe_2$	B1-WC	3.256	12.782	3.93	1.41
	PBE + D3	3.29	13.03	3.96	0.87
	exp	3.289	12.927	3.93	1.09−1.1[c]
WSe_2	B1-WC	3.284	12.900	3.93	1.67
	PBE + D3	3.28	12.99	3.96	0.96
	exp	3.268	12.925	3.96	1.2−1.44[d]
$MoTe_2$	B1-WC	3.441	13.629	3.96	1.1
	PBE + D3	3.51	14.04	4.00	0.74
	exp	3.510	13.940	3.97	0.88[e]

[a]Refs 77−79. [b]Refs 77 and 80. [c]Refs 77 and 78. [d]Refs 77 and 80. [e]Refs 81. [f]Theoretical values estimated within PBE + D3 from ref 74 and experimental lattice constants from ref 76 are included for comparison.

Table 2. Lattice Parameters a and c, the c/a Ratio, and Indirect Band Gap E_g of TMDs with the 1T Structure (Space Group $P\bar{3}m1$) Estimated within B1-WC[g]

		a (Å)	c (Å)	c/a	E_g (eV)
ZrS_2	B1-WC	3.647	5.905	1.62	1.6
	PBE + D3	3.65	5.87	1.61	0.85
	exp	3.630	5.850	1.61	1.68−1.78[a]
HfS_2	B1-WC	3.625	5.994	1.65	2.04
	PBE + D3	3.61	5.87	1.63	0.16
	exp	3.622	5.848	1.62	1.8−2.13[b]
SnS_2	B1-WC	3.656	6.046	1.65	2.41
	PBE + D2	3.68	5.89	1.60	1.27
	exp	3.649	5.899	1.63	2.07−2.48[c]
$ZrSe_2$	B1-WC	3.755	5.914	1.58	0.70
	PBE + D3	3.77	6.18	1.64	0.26
	exp	3.773	6.133	1.63	1.1−1.2[d]
$HfSe_2$	B1-WC	3.734	6.084	1.63	1.02
	PBE + D3	3.73	6.21	1.67	0
	exp	3.746	6.155	1.64	1.13[e]
$SnSe_2$	B1-WC	3.828	5.926	1.55	1.2
	PBE + D2	3.83	6.17	1.61	0.61
	exp	3.807	6.128	1.61	0.97−1.06[f]

[a]Refs 82−85. [b]Refs 82, 84, and 85. [c]Refs 82, 87, and 88. [d]Refs 83 and 86. [e]Refs 82. [f]Refs 82, 87, and 89. [g]Theoretical values estimated within PBE + D3/D2 from refs 74 and 75 and experimental lattice parameters from ref 76 are included for comparison.

the structural and electronic properties of bulk TMDs. As a result, the effect of thickness and strain on the electronic properties can be studied consistently by optimizing the structure within the same method used for transport.

The electronic band structures of bulk TMDs with 2H and 1T structures are shown in Figures 1 and 2. The indirect band gaps of 2H structures are formed between a CB minimum along the ΓK direction, a point conventionally called Λ, and a VB maximum at the Γ point (or at Λ for WTe_2) in the Brillouin zone. The top VB (resp. bottom of CB) states of 2H structures have a chalcogen p and a transition-metal d_{z^2} (resp. $d_{x^2-y^2}$ and d_{xy}) orbital character since M is trigonal bipyramidally coordinated by chalcogen atoms,[90] and the strong bonds inside the atomic layers are formed through sp^3d hybridization. The electronic band dispersions of 2H structures show similar features; the most important dissimilarities between 1T and 2H are the energy differences between (i) the CB minimum at the K point and the main CB minimum Λ, $\Delta E^{CB}_{K,\Lambda}$; and (ii) the VB maximum at the K point and the main VB maximum at the Γ point, $\Delta E^{VB}_{K,\Gamma}$ (resp. $\Delta E^{VB}_{K,\Lambda}$ for WTe_2, Figure 1). The values of $\Delta E^{CB}_{K,\Lambda}$ and $\Delta E^{VB}_{K,\Gamma}$ (resp. $\Delta E^{VB}_{K,\Lambda}$ for WTe_2) should be as small as possible to optimize TE performance (PF) through the increase of carrier pocket degeneracy. In this regard, 2H structures possess good n- or p-type PFs.

The indirect band gaps of 1T structures are formed between a CB minimum lying at the L point (or along the ML direction for SnS_2 and $SnSe_2$) and a VB maximum at Γ (or Λ for SnS_2 and $SnSe_2$). For 1T structures, the strong bonds inside the atomic layers are formed through sp^3d^2 hybridization since M is octahedrally coordinated by chalcogen atoms.[90] As a result, the top VB (resp. bottom of CB) states have a chalcogen p (resp. M t_{2g} or Sn s and p) orbital character. The electronic band dispersions show significant differences between 1T structures based on Zr (resp. Hf) and Sn (Figure 2). The 1T structures based on Zr and Hf have a second CB minimum at the A point, whereas those based on Sn have a second CB minimum at Γ. These minima are deeper in the CB and are not active in electronic transport. Moreover, only SnS_2 and $SnSe_2$ have their second VB maximum at the A point, which is close in energy to the main VB maximum Λ. SnS_2 and $SnSe_2$ have small energy differences $\Delta E^{VB}_{A,\Lambda}$ between the second and the main VB maxima, and they show the largest PF among the 1T structures.

3.2. Dependence of Electronic Properties on Thickness and Strain. The dependence of electronic band structures on thickness and strain is shown in Figure 3 for 1 ML of WSe_2, $HfSe_2$, $SnSe_2$, and in Figures S4−S6 (Supporting Information) for 1−5 MLs of WSe_2, $MoTe_2$, and $SnSe_2$. The electronic band structures depend sensitively on layer thickness (1 ML compared to bulk): the 1 ML of WSe_2 and $MoTe_2$ and all 1 MLs of the other TMDs with a 2H structure have direct band gaps at the K point in the Brillouin zone (Figures 3a, S4a, and S5a). Multiple MLs (2−5 MLs, Figures S4b−e and S5b−e) show indirect band gaps between CB minima at the Λ point and VB maxima at Γ, similar to bulk TMDs with the 2H structure. The 1−5 MLs of $SnSe_2$ and all MLs of the other TMDs with the 1T structure show indirect band gaps between a CB minimum lying at the M point or along the ΓM direction and a VB maximum lying along ΓM or ΓK similar to bulk TMDs with the 1T structure (Figure S6a−e).

The electronic properties of TMDs depend significantly on the applied in-plane strain due to the mixed hybridized nature of both band edges. In ML of 2H structures, the top VB states near Γ are shifted down in energy below the highest states at K, with a direct band gap at the K point (Figure 3a). For 2H structures, a compressive in-plane strain shifts the top VB states near the Γ point down in energy and the lowest CB states along the KH direction up (Figure 3b,c), whereas tensile strain has an opposite effect (Figure 3c,d). For 1T structures, the compressive in-plane strain (1) shifts the degenerate electronic VB at Γ up in energy, such that it becomes the main VB maximum, and (2) shifts the CB minimum at L down in energy (Figure 3f,g), whereas tensile strain has the opposite

https://doi.org/10.1021/acs.jpcc.1c07088
J. Phys. Chem. C XXXX, XXX, XXX−XXX

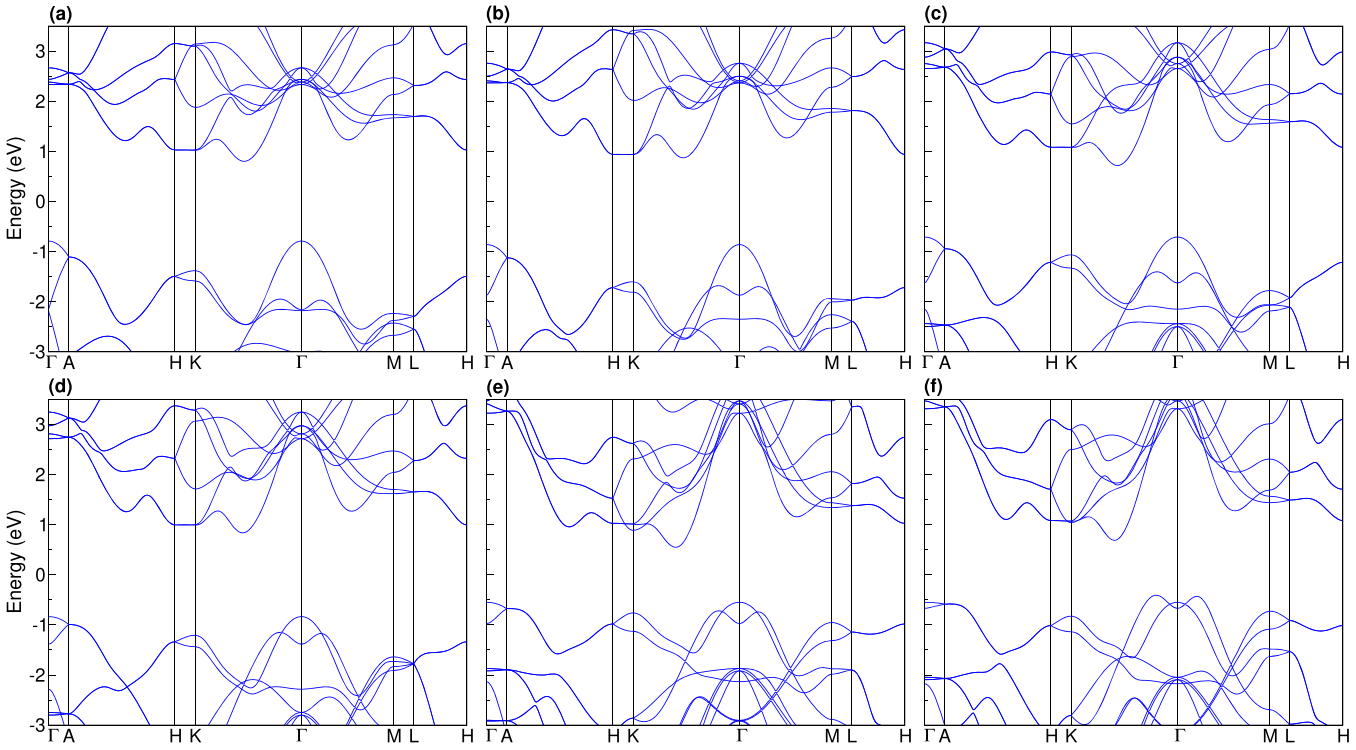

Figure 1. Electronic band structure within B1-WC for bulk (a) MoS_2, (b) WS_2, (c) $MoSe_2$, (d) WSe_2, (e) $MoTe_2$, and (f) WTe_2.

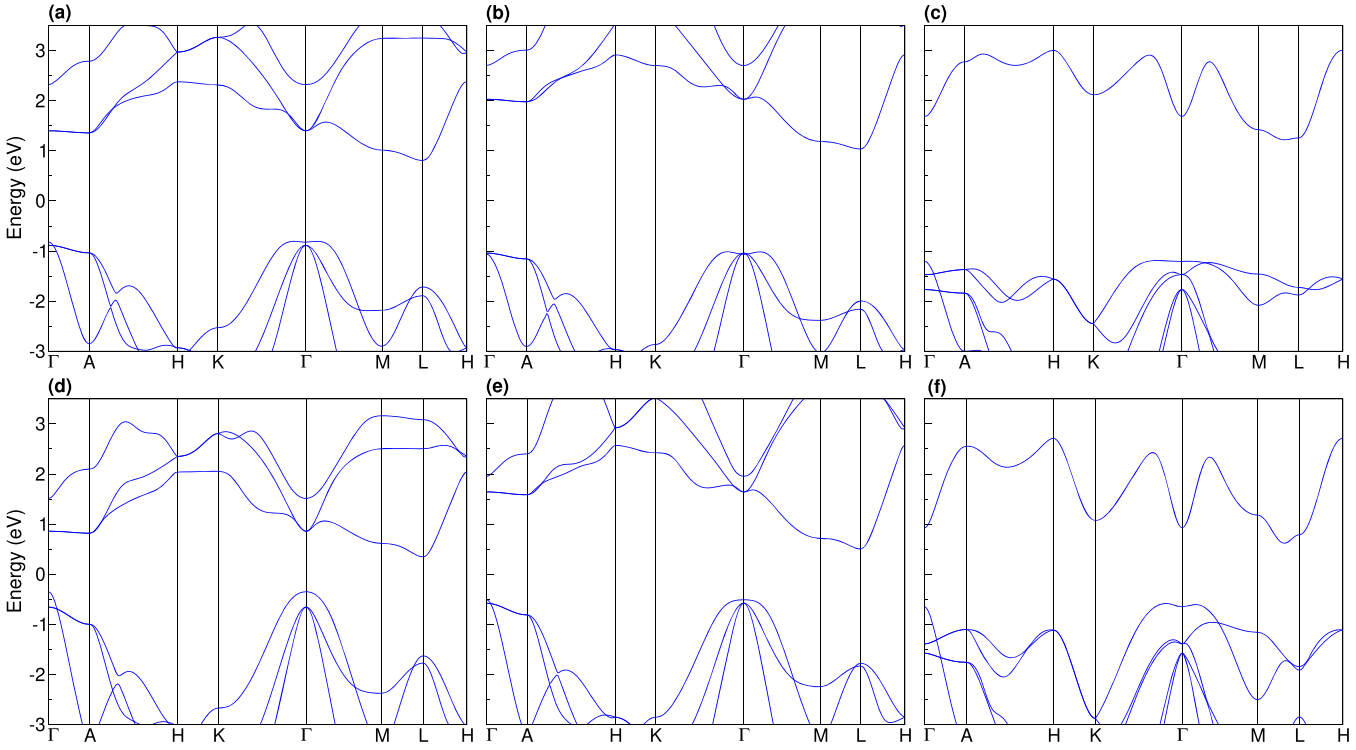

Figure 2. Electronic band structure within B1-WC for bulk (a) ZrS_2, (b) HfS_2, (c) SnS_2, (d) $ZrSe_2$, (e) $HfSe_2$, and (f) $SnSe_2$.

effect (Figure 3g,h). The position of the degenerate CB at Γ is also affected by the in-plane strain. In the case of 1 ML, the VB maximum at the Γ point is significantly lowered in energy (∼1 eV) with respect to 1T bulk structures, and it lies at ∼−1.5 eV in the VB (Figure 3e,h). For SnS_2 and $SnSe_2$, the compressive strain shifts the VB maximum along ΓK down in energy and CB states near Γ up in energy (Figure 3j,k), whereas tensile strain has the opposite effect (Figure 3k,l). The electronic band that forms the VB maximum of SnS_2 and $SnSe_2$ is significantly lowered in 1 MLs, ∼−2.2 eV in VB. The compressive in-plane strain has a similar effect with the quantum confinement in SnS_2 and $SnSe_2$ 1T structures.

We analyze more carefully the nature of the band edges of TMDs, in terms of the interplay between σ and π in-plane X−

https://doi.org/10.1021/acs.jpcc.1c07088
J. Phys. Chem. C XXXX, XXX, XXX−XXX

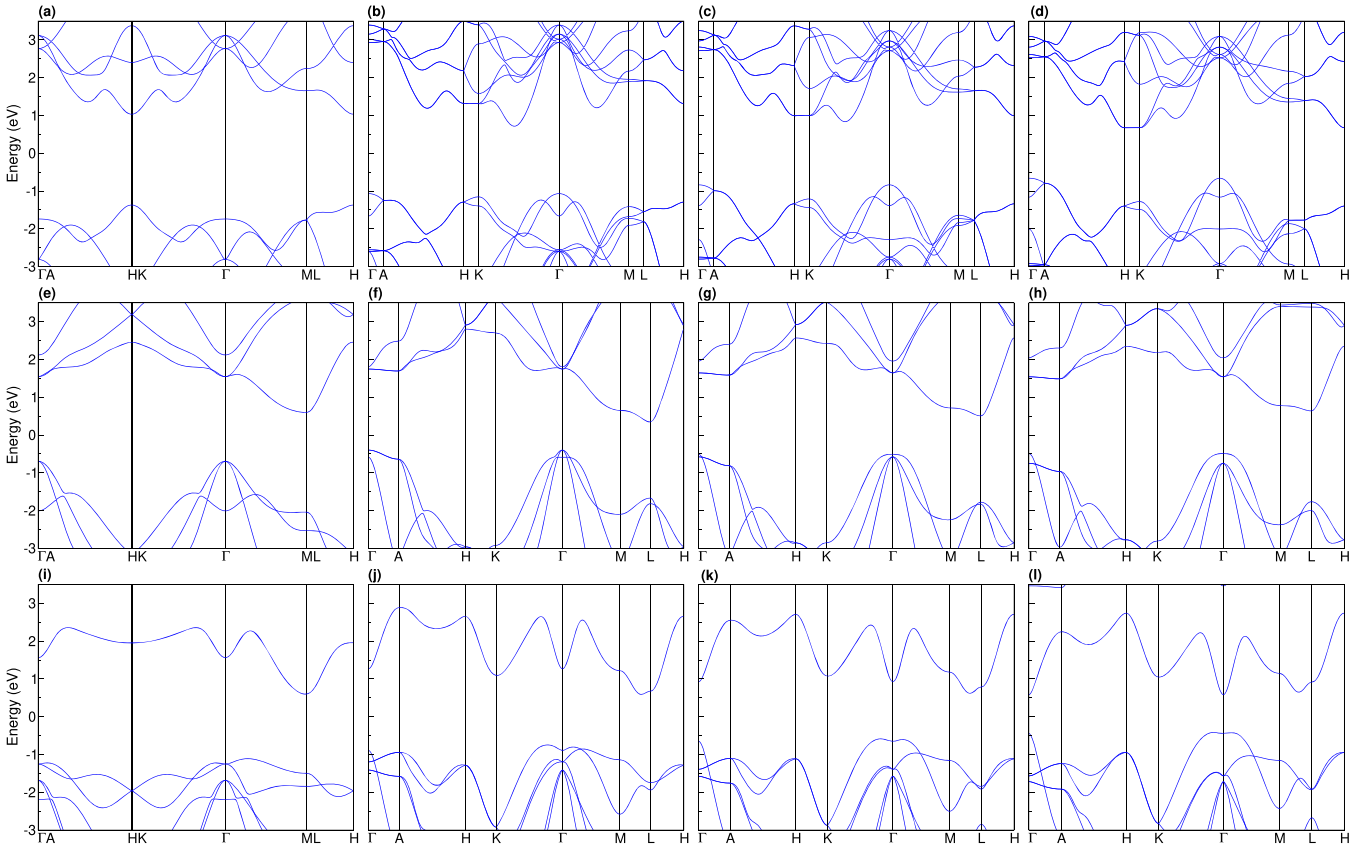

Figure 3. Electronic band structure estimated within B1-WC of: WSe_2 (a) monolayer (ML), (b) −2% strained, (c) bulk, and (d) 2% strained; $HfSe_2$ (e) 1 ML, (f) −2% strained, (g) bulk, and (h) 2% strained; and $SnSe_2$ (i) 1 ML, (j) −2% strained, (k) bulk, and (l) 2% strained.

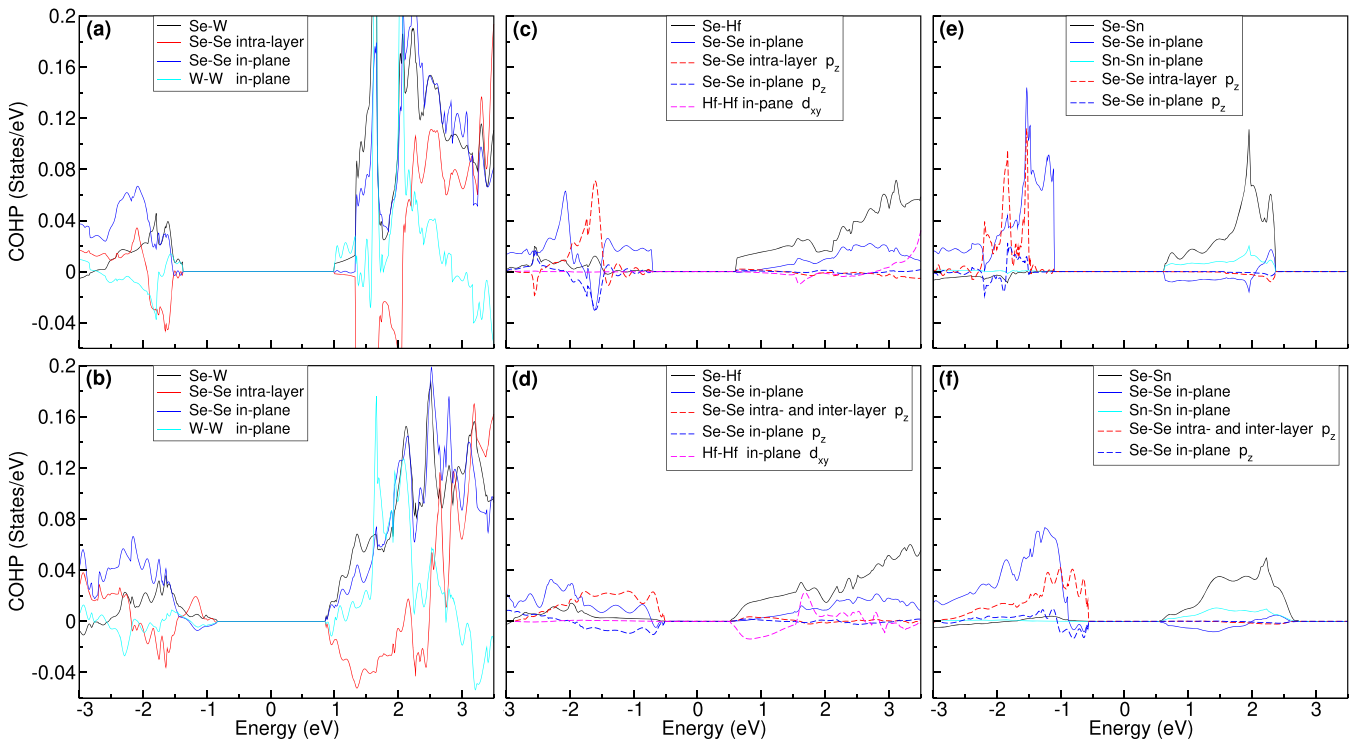

Figure 4. Crystal orbital Hamilton population (COHP) method to extract bonding information for different pairs of atoms and their orbital contributions in the (a) WSe_2 monolayer (ML), (b) WSe_2 bulk, (c) $HfSe_2$ ML, (d) $HfSe_2$ bulk, (e) $SnSe_2$ ML, and (f) $SnSe_2$ bulk. Se p_z and Hf d_{xy} orbital contributions are shown in dashed lines.

https://doi.org/10.1021/acs.jpcc.1c07088
J. Phys. Chem. C XXXX, XXX, XXX−XXX

Table 3. Effective Masses $m_{ii}(m_e)$ ($i = x, y$ Orthogonal Directions, and m_e = Free Electron Mass), Carrier Pocket Degeneracy (or Band Multiplicity) N_v, and 2D Effective Mass Quality Factor $B_m^{2D} = N_v^2$ for CB Minima and VB Maxima of WSe_2 1−2 MLs[a]

	conduction band (CB), n-type doping							valence band (VB), p-type doping						
	extremum point, its localization	m_{xx}	m_{yy}	m_{zz}	R	N_v	$B_m^{2D}/B_{m,ab}$	extremum point, its localization	m_{xx}	m_{yy}	m_{zz}	R	N_v	$B_m^{2D}/B_{m,ab}$
WSe_2 1 ML	K(1/3,1/3,0)	0.37	0.38			2	4	K(1/3,1/3,0)	0.51	0.52			2	4
	Λ(0.18,0.18,0), +0.32	0.44	0.38			6	36	Γ(0,0,0), −0.37	4.54	4.54			1	1
								M(1/2,0,0), −0.40	0.80	0.06			3	9
WSe_2 2 ML	K(1/3,1/3,0)	0.30	0.31			2	4	Γ(0,0,0)	1.39	1.39			1	1
		0.47	0.46			2	4	K(1/3,1/3,0), −0.35	0.50	0.52			2	4
	Λ(0.18,0.18,0), +0.04	0.43	0.38			6	36	K(1/3,1/3,0), −0.47	0.50	0.52			2	4
WSe_2 bulk +1% strain	Λ(0.18,0.18,0), +0.06	0.42	0.37	0.46	1.2	6	21.1	Γ(0,0,0)	0.6	0.6	1.72	2.9	1	1.4
	K(1/3,1/3,0)	0.49	0.47	138	287.6	2	21	K(1/3,1/3,0), −0.51	0.45	0.47	1.29	2.8	2	4.5
	H(1/3,1/3,1/2), +0.002	0.32	0.33	5.51	17	2	8.2	A(0,0,1/2), −0.15	1.32	1.31	0.04	0.03	1	0.3
WSe_2 bulk −2% strain	Λ(0.19,0.19,0)	0.37	0.34	0.37	1	6	19.8	Γ(0,0,0)	0.96	0.96	1.31	1.4	1	1.1
	K(1/3,1/3,0), +0.56	0.49	0.51	14.4	28.8	2	9.7	K(1/3,1/3,0), −0.09	0.52	0.53	1.1	2.1	2	4.1
	K(1/3,1/3,0), +0.56	0.23	0.24	377.9	1608	2	37.2	A(0,0,1/2), −0.19	4.5	4.6	0.03	0.01	1	0.2
	H(1/3,1/3,1/2), +0.59	0.41	0.41	3.0	3.7	2	4.9							
WSe_2 bulk	Λ(0.19,0.19,0)	0.40	0.36	0.42	1.1	6	20.1	Γ(0,0,0)	0.69	0.69	1.60	2.3	1	1.3
	K(1/3,1/3,0), +0.16	0.42	0.42	39.0	93	2	14.4	K(1/3,1/3,0), −0.37	0.48	0.49	1.21	2.5	2	4.3
	H(1/3,1/3,1/2), +0.16	0.35	0.55	9.2	21	2	8.8	A(0,0,1/2), −0.16	2.17	2.08	0.04	0.02	1	0.3

[a]Effective masses $m_{ii}(m_e)$ ($i = x, y, z$), carrier pocket degeneracy N_v, anisotropy ratio $R = m_{zz}/(m_{xx}m_{yy})^{1/2}$, and effective mass quality factor $B_{m,ab} = N_v^{5/3} R^{1/3}$ in the ab plane, for CB minima and VB maxima of WSe_2 strained and unstrained bulk. The extremum points are specified in the fraction of primitive reciprocal space vectors k_j ($j = 1-3$), and their localization in electronvolt is relative to CB minimum and VB maximum.

X (M−M) bonding through sp^2 hybridization and the strong M−X bonding inside MX_2 layers. We use the crystal orbital Hamilton population (COHP) method to extract the bonding information for different pairs of atoms and their orbital contributions.[91] Figure S8 shows COHP for M−Se and Se−Se intralayer bonding, Se−Se interlayer bonding (van der Waals), and Se−Se and M−M in-plane bonding through sp^2 hybridization in the ab plane (see Figure S7 for Se−Se interactions). In the case of bulk structures, all of these pairs of atoms have contributions to the top VB (resp. bottom CB) states through antibonding and bonding interactions (Figure S8). There are significant differences between the WSe_2 bulk and 1 ML: the states responsible for in-plane and intralayer Se−Se interactions of WSe_2 1 ML are better stabilized in energy compared to the WSe_2 bulk, being localized below −1.5 eV in the VB and above 1.3 eV in the CB (Figure 4a,b). The 1 MLs of $HfSe_2$ and $SnSe_2$ also have p_z contributions to VB states from the π in-plane Se−Se bonding and π^* intralayer Se−Se antibonding interactions lower in energy by −1.5 eV compared to the bulk (Figure 4c−f). The d_{xy} contributions to CB states from σ (resp. σ^*) in-plane Hf−Hf interactions of $HfSe_2$ 1 ML are shifted up in energy above 1.5 eV (resp. 3eV) (Figure 4c,d). The COHP analysis shows that the in-plane Se−Se and M−M bonding interactions achieved through the sp^2 hybridization and intralayer Se−Se bonding can be significantly affected by the quantum confinement and applied epitaxial strain.

3.3. Effective Masses and Anisotropy of TMD Electronic Bands. It is important to look in a more quantitative way at the effect of anisotropy and degeneracy of electronic bands on TE performance (ZT and quality factor B). For this reason, we introduce the effective mass quality factor B_m, which is directly proportional to B. Large B_m values maximize ZT at a given constant density of states effective mass m_d = const., which translate to a constant carrier density n at a given T (Supporting Information). For cubic materials and other trigonal materials having ellipsoidal pockets tilted with respect to crystallographic directions, B_m is defined as

$$B_m = \frac{N_v m_d}{m_I} = \frac{1}{3} N_v^{5/3} R^{1/3}\left(2 + \frac{1}{R}\right) \quad (2)$$

where m_I is inertial or conductivity mass ($m_c = m_I$), N_v is the band multiplicity/degeneracy, and $R = m_l/m_t$ is the band anisotropy ratio between longitudinal and transverse effective masses of the ellipsoidal carrier pockets. In the case of highly anisotropic TMDs, the longitudinal ellipsoidal axis is parallel to the c crystallographic direction such that the effective mass

https://doi.org/10.1021/acs.jpcc.1c07088
J. Phys. Chem. C XXXX, XXX, XXX−XXX

Table 4. Effective Masses $m_{ii}(m_e)$ ($i = x, y$ Orthogonal Directions, and m_e = Free Electron Mass), Carrier Pocket Degeneracy (or Band Multiplicity) N_v, and 2D Effective Mass Quality Factor $B_m^{2D} = N_v^2$ for CB Minima and VB Maxima of $SnSe_2$ 1−2 MLs[a]

	Conduction band (CB), n-type doping							Valence band (VB), p-type doping						
	extremum point, its localization	m_{xx}	m_{yy}	m_{zz}	R	N_v	$B_m^{2D}/B_{m,ab}$	extremum point, its localization	m_{xx}	m_{yy}	m_{zz}	R	N_v	$B_m^{2D}/B_{m,ab}$
$SnSe_2$ 1 ML	M(1/2,0,0)	0.60	0.39			3	9	ΓM(0.14,0,0)	1.25	0.53			6	36
								Γ(0,0,0), −0.14	0.33	0.33			1	1
$SnSe_2$ 2 ML	M(1/2,0,0)	0.70	0.41			3	9	ΓM(0.15,0,0)	1.36	0.51			6	36
	M(1/2,0,0), +0.27	0.66	0.44			3	9	Γ(0,0,0), −0.16	0.31	0.31			1	1
								Λ(0.13,0.13,0), −0.07	1.51	1.67			6	36
$SnSe_2$ bulk +2% strain	ML(0.57,0,0.34)	0.57	0.37	0.25	0.5	6	15.7	Λ(0.05,0.05,0)	1.57	1.7	0.19	0.1	6	9.2
	Γ(0,0,0), +0.12	0.1	0.1	0.11	1.1	1	1	A(0,0,1/2), −0.66	4.83	5.7	2.22	0.4	1	0.7
	K(1/3,1/3,0), +0.61	0.78	0.78	0.33	0.4	2	2.3		0.21	0.21	2.22	10.6	1	2.2
$SnSe_2$ bulk −2% strain	ML(0.55,0,0.35)	0.52	0.34	0.30	0.7	6	17.6	ΓL(0.15,0,0.14)	1.06	0.43	1.42	2.1	6	25.4
	Γ(0,0,0), +0.79	0.11	0.11	0.14	1.3	1	1.1	Λ(0.08,0.08,0), −0.02	1.52	1.39	0.36	0.3	6	13.3
	K(1/3,1/3,0), +0.58	0.58	0.58	0.32	0.6	2	2.7	A(0,0,1/2), −0.14	6.75	4.28	2.37	0.4	1	0.7
									0.18	0.18	2.37	13.2	1	2.4
$SnSe_2$ bulk	ML(0.56,0,0.34)	0.55	0.36	0.27	0.6	6	16.7	Λ(0.07,0.07,0)	1.13	1.32	0.27	0.2	6	11.6
	Γ(0,0,0), +0.45	0.11	0.11	0.12	1.1	1	1	A(0,0,1/2), −0.41	9.19	3.24	2.18	0.4	1	0.7
									0.19	0.19	2.18	11.5	1	2.3
	K(1/3,1/3,0), +0.56	0.64	0.64	0.32	0.5	2	2.5							

[a]Effective masses $m_{ii}(m_e)$ ($i = x, y, z$), carrier pocket degeneracy N_v, anisotropy ratio $R = m_{zz}/(m_{xx}m_{yy})^{1/2}$, and effective mass quality factor $B_{m,ab} = N_v^{5/3} R^{1/3}$ in the ab plane, for CB minima and VB maxima of $SnSe_2$ strained and unstrained bulk. The extremum points are specified in the fraction of primitive reciprocal space vectors k_j ($j = 1-3$), and their localization in eV is relative to CB minimum and VB maximum.

quality factors $B_{m,ab}$ (resp. $B_{m,c}$) for transport in the ab plane (resp. along the c direction) of the TMD bulk and B_m^{2D} of TMD MLs are defined as (Supporting Information)

$$B_{m,ab} = \frac{N_v m_d}{m_t} = N_v^{5/3} R^{1/3} \quad (3)$$

$$B_{m,c} = \frac{N_v m_d}{m_l} = N_v^{5/3} R^{-2/3} \quad (4)$$

$$B_m^{2D} = \frac{N_v m_d^{2D}}{m_t} = N_v^2 \quad (5)$$

where $m_l = m_{zz}$, $m_t = (m_{xx}m_{yy})^{1/2}$, $R = m_{zz}/(m_{xx}m_{yy})^{1/2}$, and $m_d^{2D} = N_v(m_{xx}m_{yy})^{1/2}$ is the 2D density of states effective mass of TMD MLs given in terms of orthogonal effective masses.

Tables 3 and 4 show the effective masses m_{ii} ($i = x, y, z$) of charge carriers, anisotropy ratio R for bulk structures, multiplicity N_v of electronic bands (resp. degeneracy of carrier pockets), and effective mass quality factors B_m^{2D} and B_m for carrier pockets of 1−2 MLs and strained (unstrained) bulk structures of WSe_2 and $SnSe_2$. These values were also estimated for extremum points located up to 0.8 eV above (below) the main minimum (maximum) of CB (VB) to compare the effect of strain. Secondary valleys located up to ∼0.5 eV from the CB minimum and the VB maximum can still be active in electronic transport at high T and large carrier concentrations. The effective masses $m_{xx}(m_{yy})$ for CB minima at K and Λ points of WSe_2 1−2 MLs are in the range 0.3−0.47m_e, comparable to those of WSe_2 bulk (0.36−0.42m_e). The strain affects $m_{xx}(m_{yy})$ values only slightly but significantly changes the energy position of CB minima. For the +1% strain, all three CB minima at K, Λ, and H points are close in energy and contribute to electronic transport and, together with the large $B_{m,ab} \sim 21$ and $R \sim 290$ values, produce an increase in TE performance. In the case of p-type doping, $m_{xx}(m_{yy})$ around the maximum at K point for WSe_2 1−2 MLs is ∼0.5m_e, comparable to that of the WSe_2 bulk. For the maximum at Γ, $m_{xx}(m_{yy})$ values are ∼1.4−4.5m_e, quite higher than that of the WSe_2 bulk (∼0.7m_e). The applied epitaxial strain to the WSe_2 bulk significantly changes the position of maxima at K and Γ points. A compressive strain of ∼−2% increases the degeneracy of these two maxima, resulting in an enhanced p-type TE performance of WSe_2 with $B_{m,ab} \sim 4$ and $R \sim 2$ at K maximum.

The M valley effective masses $m_{xx}(m_{yy})$ of $SnSe_2$ 1−2 MLs around the minimum at M point have values in the range of 0.39−0.70m_e, slightly higher than those corresponding in the ML direction of the $SnSe_2$ bulk. Strain applied to the $SnSe_2$ bulk does not significantly change the effective masses of CB minima along the ML direction and at Γ and K points. As in WSe_2, the applied strain significantly changes the energy position of the CB minimum of $SnSe_2$ and other TMDs. A strain slightly higher than +2% increases the energy degeneracy of minima along the ML direction ($B_{m,ab} \sim 16$) and at the Γ point, enhancing only slightly the TE performance for n-type doping. In the case of p-type doping, $m_{xx}(m_{yy})$ values of $SnSe_2$ 1−2 MLs for the VB maximum along the ΓM direction are

https://doi.org/10.1021/acs.jpcc.1c07088
J. Phys. Chem. C XXXX, XXX, XXX−XXX

slightly smaller than for the Λ maximum of the $SnSe_2$ bulk. The strain modifies the effective masses of maxima along the ΓL direction and at Λ and A points and also the energy positions of these maxima with respect to the top of VB. A −2% strain puts the main maximum along ΓL ($B_{m,ab} \sim 25$, $R \sim 2$), which is almost degenerate with Λ ($B_{m,ab} \sim 13$, $R \sim 0.3$), and moves to ∼−0.14 eV the anisotropic hole pocket at the A point ($B_{m,ab} \sim 2$, $R \sim 13$). All of these maxima are active in hole transport and responsible for the very good p-type TE properties of the $SnSe_2$ bulk under a compressive strain of −2%. We also estimate B_m and R values for PbTe and Bi_2Te_3 to compare with those of high-potential TMDs. Equation 2 gives $B_m = 15$ using $R = 9.6$ for n-type PbTe[92,93] and $B_m = 28$ using $R = 7.6$ for n-type Bi_2Te_3.[94,95] For the main CB minima of n-type doped WSe_2 and $SnSe_2$, $B_{m,ab}$ values are comparable to those of n-type PbTe and Bi_2Te_3, whereas the anisotropy ratio R is much weaker for TMDs.

3.4. Thermoelectric Property Dependence on Thickness and Strain. In the constant relaxation time approximation, the relaxation time τ is considered independent of energy and T, and $\tau = \tau_0$ is estimated by fitting the experimental values of electrical conductivity σ^{exp} at a given carrier concentration n and T. The relaxation time within B1-WC was determined by fitting σ_a^{exp} values measured in the *ab* plane of TMD monocrystalline materials at different n values and 300 K (see Table 5). The value of τ_a in the *a* direction for n-type doping is ∼1×10^{-14} s, and this value was used in the study of TE properties of TMDs. The electrical conductivities σ_c^{exp} measured in the *c* direction are 2 orders of magnitude smaller than σ_a^{exp} ($\sigma_c^{exp}/\sigma_a^{exp} \sim 0.01$).[97,98] By fitting σ_c^{exp}, the relaxation time τ_c is ∼1×10^{-16} s. This confirms that the preferential transport direction is along TMD layers (*ab* plane). Many TMDs including sulfides, $MoSe_2$, $ZrSe_2$, and $HfSe_2$ have in-plane lattice/phonon thermal conductivities $\kappa_{l,a}$ larger than 10 W/(m K) at 300 K,[100] which will reduce their ZT. The dependence of the TE properties on thickness and strain is studied for the most promising TMDs (WSe_2,[100] $MoTe_2$,[100100] and $SnSe_2$[101,102]), which also have $\kappa_{l,a}$ values smaller than 10 W/(m K) at 300 K.

Table 5. Relaxation Time τ_a Estimated within B1-WC by Fitting the Electrical Conductivity σ_a^{exp} Measured in the *ab* Plane of $SnSe_2$, $MoSe_2$, and MoS_2 Monocrystalline Materials at Different Carrier Concentrations n and 300 K

	σ^{exp} (S/m)	n (cm^{-3})	τ_a (10^{-14} s)
$SnSe_2$ tip-n[a]	100	2×10^{17}	0.48
$MoSe_2$ tip-n[b]	20	3.5×10^{16}	1.04
MoS_2 tip-n[b]	3	6×10^{15}	1.04
WSe_2 tip-p[b]	600	3×10^{17}	3.9

[a]Ref 96. [b]Ref 97.

The PF values estimated as a function of the chemical potential μ at 300 K for 1−3 MLs and strained/unstrained bulk structures of WSe_2, $MoTe_2$, and $SnSe_2$ are shown in Figures S9−S11. The dependence on layer thickness and strain for the power factor component PF_{xx} along the *a* direction, estimated at experimentally accessible optimal μ values, is summarized in Figure 5. The PF_{xx} of WSe_2 1−3 MLs has values of ∼1.2−6 mW/(m K^2) at optimal $\mu \sim 1$−1.4 eV relative to the middle of the band gap, which corresponds to μ lying near the CB minimum, at K (1 ML) or Λ (2−3 MLs) points (Figure S4a−c). The maximum PF_{xx} of ∼6 mW/(m K^2) is found in the 2 ML structure by increasing the energy degeneracy of CB minima at K and Λ points (Figure S4b). This maximum value of ∼6 mW/(m K^2) is comparable to that of Bi_2Te_3 (PF ∼ 5−6 mW/(m K^2) at 300 K). PF_{xx} values of ∼1.2−6 mW/(m K^2) at 300 K for WSe_2 1−3 MLs are comparable to the estimated experimental values of ∼4 mW/(m K^2) (∼3 mW/(m K^2)) for p-type (n-type) gate-doped ultrathin WSe_2 single crystals consisting of ∼1−2 MLs.[99] For WSe_2 1 ML, a theoretical value of ∼0.86 mW/(m K^2) (∼0.83 mW/(m K^2)) was estimated for n-type (p-type) doping at 300 K.[42] In the case of strained bulk WSe_2, PF_{xx} was ∼3.2 mW/(m K^2) at optimal $\mu \sim 0.8$ eV and a tensile strain of +1% (Figures 5 and S9f). PF_{xx} of the WSe_2 bulk is ∼2.9 mW/(m K^2), comparable to that of PbTe at 300 K (Figures 5 and S9e). For p-type doping at optimal $\mu \sim -1.4$eV, PF_{xx} is ∼2.8 mW/(m K^2) for 1 ML and ∼3.8 mW/(m K^2) for bulk WSe_2 under a compressive strain of −2% (Figures 5 and S9a,d).

The n-type PF_{xx} of $MoTe_2$ 1−3 MLs is ∼2.7−5.8 mW/(m K^2) at optimal $\mu \sim 0.8$−1 eV (Figures 5 and S10a−c). The maximum PF_{xx} of ∼5.8 mW/(m K^2) corresponds to the 1 ML structure, achieved through the energy degeneracy of CB minima at K and Λ points (Figure S5a). For $MoTe_2$ 1 ML, also a theoretical value of ∼0.97 mW/(m K^2) (∼1.06 mW/(m K^2)) was estimated for n-type (p-type) doping at 300 K.[42] A tensile strain of +2% almost doubles the n-type PF_{xx} of the $MoTe_2$ bulk from ∼1.6 to ∼2.9 mW/(m K^2) (Figures 5 and S10e,f), while a compressive strain of −2% increases the p-type PF_{xx} of the $MoTe_2$ bulk from ∼2.1 to ∼2.6 mW/(m K^2) (Figures 5 and S10d,e). The n-type PF_{xx} of $SnSe_2$ 1−3 MLs has values of ∼1.4−3.1 mW/(m K^2) at optimal $\mu \sim 0.7$−0.8 eV (Figures 5 and S11a−c). The maximum PF_{xx} of ∼3.1 mW/(m K^2) corresponds to a 3 ML structure, being achieved by the contribution in transport of a very anisotropic band at the M point, which forms the CB minimum (Figure S6c). The maximum n-type PF_{xx} value of ∼1.6 mW/(m K^2) for the $SnSe_2$ bulk is similar to the maximum experimental value of ∼1.2 mW/(m K^2) measured in n-type doped $SnCu_{0.005}Se_{1.98}Br_{0.02}$ polycrystals nanostructured through grinding and spark plasma sintering (SPS) in which Cu intercalates between $SnSe_2$ layers according to transmission electron microscopy (TEM) analysis[103] and smaller than the values of ∼0.8 mW/(m K^2) for n-type doped $SnSe_{1.98}Br_{0.02}$ SPS nanostructured polycrystals,[103] ∼0.8 mW/(m K^2) for n-type doped $SnSe_{1.95}Cl_{0.015}$ SPS pellets of oriented nanoplates,[104] and ∼0.35 mW/(m K^2) for n-type doped $Sn_{0.99}Ag_{0.01}Se_2$ SPS nanostructured polycrystals at 773 K.[105] Theoretical n-type PF_{xx} values of ∼0.38 and ∼15.6 mW/(m K^2) for the $SnSe_2$ bulk were estimated using a smaller value of $\tau_a = 0.128 \times 10^{-14}$ s fitted on σ_a^{exp} of $SnSe_2$ single crystals[36] and a larger theoretical value of $\tau_a = 6.9 \times 10^{-14}$ s at 300 K.[37] The −2% compressive strain increases the p-type PF_{xx} of the $SnSe_2$ bulk by a factor of ∼5.6, from ∼0.8 to ∼4.5 mW/(m K^2) for the optimal doping that can be achieved experimentally at $\mu \sim -0.6$ eV (Figures 5 and S11d,e).

At high T ($T > 600$ K), the constant relaxation time approximation overestimates the PF. We went beyond this approximation considering a $1/T$ temperature dependence for relaxation times due to the scattering of charge carriers by acoustic and optical phonons, which are dominant at high T.[30] PF values estimated as a function of μ at 800 K for 1−3 MLs and strained/unstrained bulk structures of WSe_2, $MoTe_2$, and $SnSe_2$ are shown in Figures S12−S14. PF_{xx} dependence on layer thickness and strain estimated at optimal μ values and

https://doi.org/10.1021/acs.jpcc.1c07088
J. Phys. Chem. C XXXX, XXX, XXX−XXX

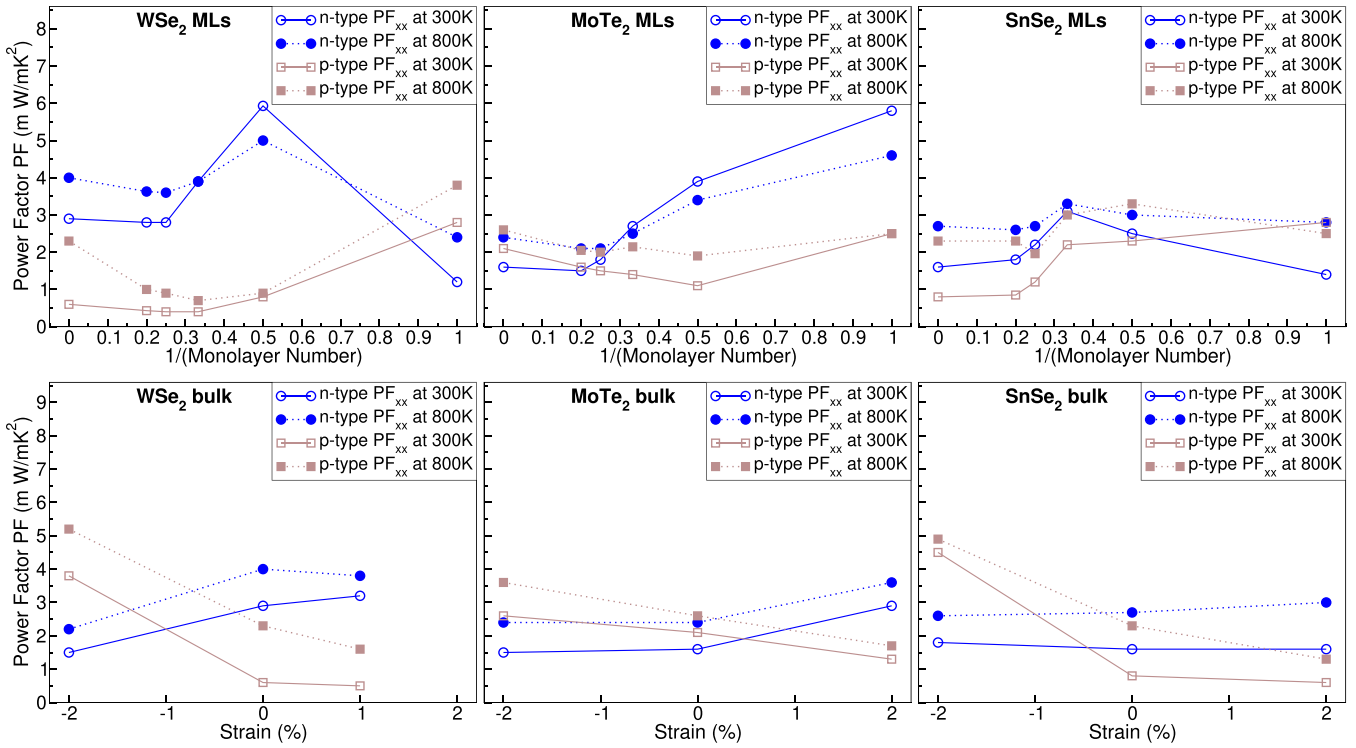

Figure 5. Power factor PF_{xx} dependence on the inverse of the ML number and strain for MLs and bulk structures of WSe_2, $MoTe_2$, and $SnSe_2$, estimated at experimentally accessible optimal chemical potential μ values within B1-WC at 300 K using the relaxation time $\tau_a = 1 \times 10^{-14}$ s and at 800 K using $1/T$ temperature dependence of the acoustic and optical relaxation times. n-Type and p-type PF_{xx} components in the *a* direction are represented by symbols, which are joined by lines to guide the eye.

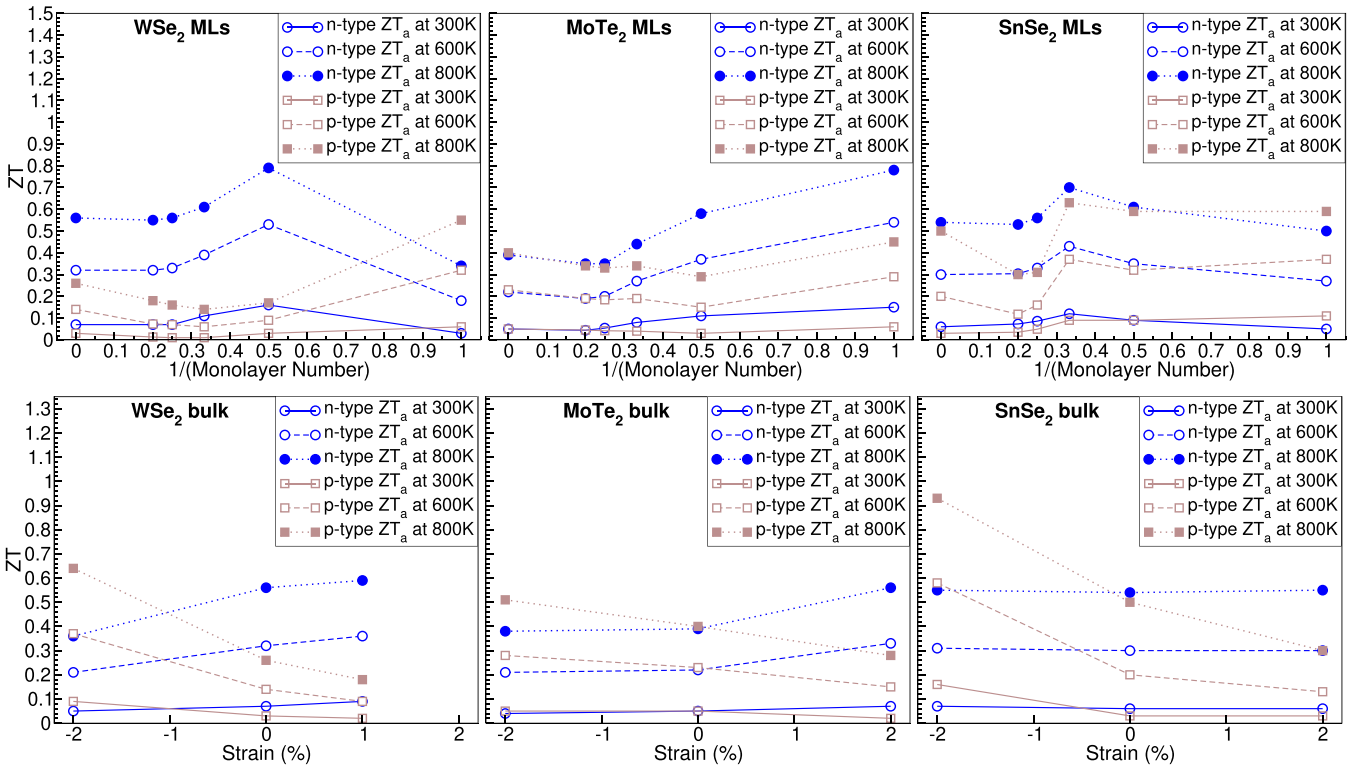

Figure 6. Figure-of-merit ZT_a dependence on the inverse of the ML number and strain for MLs and bulk structures of WSe_2, $MoTe_2$, and $SnSe_2$, estimated at experimentally accessible optimal chemical potential μ values within B1-WC at 300, 600, and 800 K. n-Type and p-type ZT_a components in the **a** direction are represented by symbols, which are joined by lines to better see their dependence.

https://doi.org/10.1021/acs.jpcc.1c07088
J. Phys. Chem. C XXXX, XXX, XXX−XXX

800 K is also included in Figure 5. WSe_2 1−3 MLs show an n-type PF of ∼2.4−5 mW/(m K^2) at 800 K and optimal μ (Figures 5 and S12a−c). WSe_2 bulk under a +1% tensile strain has a maximum n-type PF_{xx} of ∼3.8−4 mW/(m K^2) (Figures 5 and S12f). For p-type doping, the maximum PF_{xx} at 800 K is ∼3.8 mW/(m K^2) in WSe_2 1 ML and ∼5.2 mW/(m K^2) in the WSe_2 bulk under a −2% compressive strain (Figures 5 and S12d). For $MoTe_2$ MLs and strained bulk at 800 K, the maximum n-type PF_{xx} is ∼4.6 mW/(m K^2) in $MoTe_2$ 1 ML and the maximum p-type PF_{xx} is ∼3.6 mW/(m K^2) for −2% strain (Figures 5 and S13a,d). In the case of $SnSe_2$ 1−3 MLs, the maximum n-type PF_{xx} at 800 K is comparable to that at 300 K, whereas for strained bulk $SnSe_2$, the maximum n-type PF_{xx} at 800 K is ∼3 mW/(m K^2). For p-type doping of $SnSe_2$ 1−3 MLs, the maximum PF_{xx} at 800 K is ∼3.3 mW/(m K^2), whereas for strained bulk $SnSe_2$, the maximum p-type PF_{xx} at 800 K is ∼4.9 mW/(m K^2) (Figures 5 and S14).

The dependence of ZT on layer thickness and in-plane strain for WSe_2, $MoTe_2$, and $SnSe_2$ at optimal μ values is summarized in Figure 6, while ZT(μ) values along the $a(c)$ directions are shown in Figures S15−S17. The lattice/phonon thermal conductivities $\kappa_{l,a}$ ($\kappa_{l,c}$) along the a (c) directions used in the estimation of ZT were taken from experimental or theoretical data. The values of $\kappa_{l,a}$ ($\kappa_{l,c}$) at 300, 600, and 800 K for WSe_2 are 10 W/(m K) (1.5 W/(m K)), 5 W/(m K) (0.75 W/(m K)), and 3.75 W/(m K) (0.56 W/(m K));[100] for $MoTe_2$, they are 9.8 W/(m K) (1.9 W/(m K)), 4.9 W/(m K) (0.95 W/(m K)), and 3.68 W/(m K) (0.71 W/(m K));[100] and for $SnSe_2$, they are 7.3 W/(m K) (0.8 W/(m K)), 3.65 W/(m K) (0.4 W/(m K)), and 2.74 W/(m K) (0.3 W/(m K)).[101,102] The maximum n-type ZTs at 300 K are ∼0.1−0.15 for 1−3 MLs of WSe_2, $MoTe_2$, and $SnSe_2$. The ZT values are larger than the theoretical ZT ∼ 0.005−0.075 of WSe_2 1 ML estimated at 300 K using $\kappa_{l,a}$ = 19.5 W/(m K) and considering the effect of substrate, interface phonons, and dynamic screening.[39] n-Type ZTs ∼ 0.33,[42] ∼0.9,[41] and ∼1[40] of WSe_2 1 ML and ZT ∼ 0.46 of $MoTe_2$ 1 ML[42] were estimated theoretically at 300 K using theoretical $\kappa_{l,a}$ = 0.66[42] and 0.3 W/(m K),[41] an experimental $\kappa_{l,a}$ = 34.5 W/(m K),[40] and a theoretical $\kappa_{l,a}$ = 0.54 W/(m K),[42] respectively. These larger n-type ZTs are mainly due to the smaller used $\kappa_{l,a}$, and in the case of ref 40 are due to the larger relaxation time of $\tau_a \sim 2.3 \times 10^{-12}$ s that we estimate for a 14 nm mean free path of charge carriers. Quantum confinement in 1−3 MLs of WSe_2, $MoTe_2$, and $SnSe_2$ increases the maximum ZT for n-type doping at 800 K compared to bulk structures. The maximum ZT values are ∼0.8, ∼0.8, and ∼0.7 at 800 K for 1−3 MLs of WSe_2, $MoTe_2$, and $SnSe_2$, respectively (compared to ∼0.55, ∼0.4, and ∼0.5 at 800 K for bulk WSe_2, $MoTe_2$, and $SnSe_2$, respectively). The ZT value of ∼0.5 at 800 K for the n-type $SnSe_2$ bulk agrees well with experimental values of ∼0.6 at 800 K for n-type doped $SnSe_{1.95}Cl_{0.015}$ SPS nanostructured pellets[104] and ∼0.63 at 800 K for $SnCu_{0.005}Se_{1.98}Br_{0.02}$[103] and ∼0.4 at 773 K for $Sn_{0.99}Ag_{0.01}Se_2$[105] n-type doped SPS nanostructured polycrystals. The nanostructured $SnSe_2$ polycrystals have $\kappa_{l,a}$ values of ∼0.52 W/(m K) at 800 K,[104] ∼0.98 W/(m K) at 800 K,[103] and ∼0.7 W/(m K) at 773 K,[105] which are smaller than the value of the $SnSe_2$ bulk, but at the same time, their PF_{xx} is decreased through nanostructuring. The theoretical n-type ZT values of ∼0.9[36] and ∼3[37] for the $SnSe_2$ bulk were estimated using $\kappa_{l,a}$ = 0.55[36] and ∼2.54 W/(m K).[37] The maximum ZT for p-type doped WSe_2 1 ML is ∼0.55 at 800 K. A ZT of ∼0.14 at 600 K for the p-type WSe_2 bulk compares well with experimental values of ∼0.14−0.22 measured in Nb-doped $W_{1-x}Nb_xSe_{2-y}S_y$ textured polycrystals under high-pressure pressing, which have PF ∼ 0.3−0.8 mW/(m K^2) and $\kappa_{l,a}$ ∼ 1.7−2 W/(m K) at 650 K.[106] The tensile epitaxial strain increases ZT at 800 K to ∼0.6 and ∼0.55 for n-type doped bulk structures of WSe_2 and $MoTe_2$, respectively. The compressive epitaxial strain increases p-type ZT values to ∼0.65, ∼0.55, and ∼0.9 at 800 K for bulk structures of WSe_2, $MoTe_2$, and $SnSe_2$, respectively. These ZT values of ∼0.6−0.9 at 800 K estimated in MLs and bulk structures of WSe_2, $MoTe_2$, and $SnSe_2$ under epitaxial strain are comparable to those of PbTe (ZT ∼ 0.8−1 at 650 K), highlighting the TE potential of these materials for applications at high temperatures (T ∼ 600−800 K). The epitaxial strain imposed by the substrate of films based on these high-potential TE materials is an effective way to increase the carrier pocket degeneracy, in order to exploit both the anisotropic electron pockets at the K point of WSe_2 (R ∼ 288) and $MoTe_2$ (R ∼ 64) and the A point hole pocket of $SnSe_2$ (R ∼ 13).

We also considered the explicit Nb doping at the W site in WSe_2 and Sb doping at Sn and Se sites in $SnSe_2$ using a supercell approach and performed spin-polarized calculations including nonmagnetic, ferromagnetic, and antiferromagnetic orders on the doping elements and their nearest neighbors to check the nonmagnetic ground state and spin degeneracy of WSe_2 and $SnSe_2$ doped semiconductors and the validity of TE properties as predicted by rigid band approximation for low doping levels. The explicit Nb doping in WSe_2 and Sb doping in $SnSe_2$ preserve their nonmagnetic semiconducting behavior. Nb at the W site is a p-type dopant in WSe_2, and Sb at the Sn site acts as a p-type dopant in $SnSe_2$ with the Sb ion in a 3+ charge state (Sb^{3+}), while Sb at Se sites acts as an n-type dopant with the Sb ion in a 1− charge state (Sb^{1-}), consistent with the experimental results (Figure S18).[107] The magnetism-enhanced thermoelectricity is a hot research topic,[108,109] and to study the interaction of charge carriers with localized magnetic spins, the doping of TMDs should be conducted with magnetic elements such as Mn, Fe, and Co.

4. CONCLUSIONS

The first-principles study of the TMD monolayer and bulk structures under in-plane strain shows that their electronic properties depend significantly on the layer thickness (1−3 MLs) and the applied strain. This makes them promising candidates for electronic band structure engineering: the applied in-plane strain can be used to increase the carrier pocket degeneracy of CB and VB bands and to optimize the TE properties (ZT and PF) of textured and strained thin films. The accuracy of calculated electronic and TE properties in 2D materials depends on the ability of the exchange−correlation functional to describe the structural properties (especially the c/a ratio) compared to the experiment. COHP analysis reveals that the electronic charge describing the in-plane and intralayer X−X interactions is lower in energy for single monolayers than for bulk TMDs with the 2H structure (X = S, Se, and Te), such that the carrier transport in single monolayers of 2H TMDs is mostly achieved through in-plane TM−TM and TM−X antibonding states. Single monolayers of 1T structures also have the electronic charge from p_z orbitals, which describe the π in-plane X−X bonding and π^* intralayer X−X antibonding interactions, again lower in energy compared to bulk 1T structures, such that hole transport is achieved through the σ^* in-plane X−X antibonding states with sp^2 hybridization, whereas the electron transport remains similar to that of

https://doi.org/10.1021/acs.jpcc.1c07088
J. Phys. Chem. C XXXX, XXX, XXX−XXX

bulk 1T structures. In spite of the fact that carrier pocket degeneracy can be tuned by strain and layer thickness, the effective masses $m_{xx}(m_{yy})$ in the preferential transport direction of the electron pockets are relatively large (~0.1−3.1m_e and even larger for hole pockets ~0.2−94m_e) compared to n-type PbTe[92,93] (~0.025m_e) and n-type Bi_2Te_3[94,95] (~0.06m_e), which will limit TMD carrier mobilities. Although the effective mass quality factors $B_{m,ab}$ for the main electron pockets of TMDs are comparable to B_m of PbTe and Bi_2Te_3, the anisotropy R of TMD electronic pockets is much weaker than that of PbTe and Bi_2Te_3 due to the large effective masses $m_{xx}(m_{yy})$. Another detrimental effect to TE performance of the nanostructured TMDs is their weak dielectric screening (in-plane static dielectric permittivity values of ~15, ~18, and ~10 for WSe_2, $MoTe_2$, and $SnSe_2$, respectively), which will result in scattering of carriers by grain boundary regions, decreasing the carrier mobilities of polycrystalline TMDs.[110] In this respect, the nanostructuring should be achieved through artificial heterostructures/superlattices, formed by TMDs with a high TE potential, which will allow at the same time the reduction of κ_l and the use of in-plane strain imposed by the superlattice periodicity along c. Such superlattices with large thicknesses and imposed in-plane strain are the most natural routes for practical TE applications.

■ ASSOCIATED CONTENT

Supporting Information

The Supporting Information is available free of charge at https://pubs.acs.org/doi/10.1021/acs.jpcc.1c07088.

Technical details of calculations; effect of spin−orbit interaction for 1 ML and bulk structures of WSe_2 and $SnSe_2$ (Figures S1−S3); electronic band structures for 1−5 MLs and bulk TMDs of WSe_2, $MoTe_2$, and $SnSe_2$ (Figures S4−S6); bonding information analysis (Figures S7−S8); electronic band anisotropy and effective mass quality factors B_m and B_m^{2D} (Table S1); power factor (PF) and figure-of-merit (ZT) dependences on chemical potential μ (Figures S9−S17); explicit doping of TMDs (Figure S18) (PDF)

■ AUTHOR INFORMATION

Corresponding Author

Daniel I. Bilc − *Faculty of Physics, Babeş-Bolyai University, RO-400084 Cluj-Napoca, Romania;* orcid.org/0000-0002-4298-4250; Phone: +40 264 405328; Email: Daniel.Bilc@ubbcluj.ro

Authors

Diana Benea − *Faculty of Physics, Babeş-Bolyai University, RO-400084 Cluj-Napoca, Romania*

Viorel Pop − *Faculty of Physics, Babeş-Bolyai University, RO-400084 Cluj-Napoca, Romania*

Philippe Ghosez − *Theoretical Materials Physics, Q-MAT, CESAM, Université de Liège (B5), B-4000 Liège, Belgium*

Matthieu J. Verstraete − *Nanomat, Q-Mat, CESAM, and European Theoretical Spectroscopy Facility, Université de Liège (B5), B-4000 Liège, Belgium*

Complete contact information is available at: https://pubs.acs.org/10.1021/acs.jpcc.1c07088

Notes

The authors declare no competing financial interest.

■ ACKNOWLEDGMENTS

The authors acknowledge the financial support from a grant of the Romanian National Authority for Scientific Research and Innovation, CCCDI—UEFISCDI, project number COFUND-FLAGERA II-MELoDICA, within PNCDI III. Computational resources were provided by the high-performance computational facility of Babes-Bolyai University (MADECIP, POS-CCE COD SMIS 48801/1862) cofinanced by the European Regional Development Fund.

■ REFERENCES

(1) Manzeli, S.; Ovchinnikov, D.; Pasquier, D.; Yazyev, O. V.; Kis, A. 2D transition metal dichalcogenides. *Nat. Rev. Mater.* **2017**, *2*, No. 17033.

(2) Yang, L.; Xie, C.; Jin, J.; Ali, R. N.; Feng, C.; Liu, P.; Xiang, B. Properties, preparation and applications of low dimensional transition metal dichalcogenides. *Nanomaterials* **2018**, *8*, No. 463.

(3) Pallecchi, I.; Manca, N.; Patil, B.; Pellegrino, L.; Marré, D. Review on thermoelectric properties of transition metal dichalcogenides. *Nano Futures* **2008**, *4*, No. 032008.

(4) Bertolazzi, S.; Brivio, J.; Kis, A. Stretching and breaking of ultrathin MoS_2. *ACS Nano* **2011**, *5*, 9703−9709.

(5) Mak, K. F.; McGill, K. L.; Park, J.; McEuen, P. L. The valley Hall effect in MoS_2 transistors. *Science* **2014**, *344*, 1489−1492.

(6) Zhou, B. T.; Taguchi, K.; Kawaguchi, Y.; Tanaka, Y.; Law, K. T. Spin-orbit coupling induced valley Hall effects in transition-metal dichalcogenides. *Commun. Phys.* **2019**, *2*, No. 26.

(7) Xiang, H.; Xu, B.; Liu, J.; Xia, Y.; Lu, H.; Yin, J.; Liu, Z. Quantum spin Hall insulator phase in monolayer WTe_2 by uniaxial strain. *AIP Adv.* **2016**, *6*, No. 095005.

(8) Xiao, D.; Liu, G.-B.; Feng, W.; Xu, X.; Yao, W. Coupled spin and valley physics in monolayers of MoS_2 and other group-VI dichalcogenides. *Phys. Rev. Lett.* **2012**, *108*, No. 196802.

(9) Mak, K. F.; He, K.; Shan, J.; Heinz, T. F. Control of valley polarization in monolayer MoS_2 by optical helicity. *Nat. Nanotechnol.* **2012**, *7*, 494−498.

(10) Zeng, H.; Dai, J.; Yao, W.; Xiao, D.; Cui, X. Valley polarization in MoS_2 monolayers by optical pumping. *Nat. Nanotechnol.* **2012**, *7*, 490−493.

(11) Ali, M. N.; Xiong, J.; Flynn, S.; Tao, J.; Gibson, Q. D.; Schoop, L. M.; Liang, T.; Haldolaarachchige, N.; Hirschberger, M.; Ong, N. P.; et al. Large, non-saturating magnetoresistance in WTe_2. *Nature* **2014**, *514*, 205−208.

(12) Ye, J. T.; Zhang, Y. J.; Akashi, R.; Bahramy, M. S.; Arita, R.; Iwasa, Y. Superconducting dome in a gate-tuned band insulator. *Science* **2012**, *338*, 1193−1196.

(13) Hsu, Y.-T.; Vaezi, A.; Fischer, M. H.; Kim, E.-A. Topological superconductivity in monolayer transition metal dichalcogenides. *Nat. Commun.* **2017**, *8*, No. 14985.

(14) Kang, D.; Zhou, Y.; Yi, W.; Yang, C.; Guo, J.; Shi, Y.; Zhang, S.; Wang, Z.; Zhang, C.; Jiang, S.; et al. Superconductivity emerging from a suppressed large magnetoresistant state in tungsten ditelluride. *Nat. Commun.* **2015**, *6*, No. 7804.

(15) Pan, X.; Chen, X.; Liu, H.; Feng, Y.; Wei, Z.; Zhou, Y.; Chi, Z.; Pi, L.; Yen, F.; Song, F.; et al. Pressure-driven dome-shaped superconductivity and electronic structural evolution in tungsten ditelluride. *Nat. Commun.* **2015**, *6*, No. 7805.

(16) Lu, P.; Kim, J.; Yang, J.; Gao, H.; Wu, J.; Shao, D.; Li, B.; Zhou, D.; Sun, J.; Akinwande, D.; et al. Origin of superconductivity in the Weyl semimetal under pressure. *Phys. Rev. B* **2016**, *94*, No. 224512.

(17) Ang, R.; Wang, Z. C.; Chen, C. L.; Tang, J.; Liu, N.; Liu, Y.; Lu, W. J.; Sun, Y. P.; Mori, T.; Ikuhara, Y. Atomistic origin of an ordered superstructure induced superconductivity in layered chalcogenides. *Nat. Commun.* **2015**, *6*, No. 6091.

(18) Zhang, W.; Huang, Z.; Zhang, W.; Li, Y. Two-dimensional semiconductors with possible high room temperature mobility. *Nano Res.* **2014**, *7*, 1731−1737.

(19) Ma, N.; Jena, D. Charge scattering and mobility in atomically thin semiconductors. *Phys. Rev. X* **2014**, *4*, No. 011043.
(20) Wang, Y.; Sohier, T.; Watanabe, K.; Taniguchi, T.; Verstraete, M. J.; Tutuc, E. Electron mobility in monolayer WS_2 encapsulated in hexagonal boron-nitride. *Appl. Phys. Lett.* **2021**, *118*, No. 102105.
(21) Zhang, H.; Liu, C.-X.; Qi, X.-L.; Dai, X.; Fang, Z.; Zhang, S.-C. Topological insulators in Bi_2Se_3, Bi_2Te_3 and Sb_2Te_3 with a single Dirac cone on the surface. *Nat. Phys.* **2009**, *5*, 438−442.
(22) Hasan, M. Z.; Kane, C. L. Colloquium: topological insulators. *Rev. Mod. Phys.* **2010**, *82*, 3045−3067.
(23) Qi, X.-L.; Zhang, S.-C. Topological insulators and superconductors. *Rev. Mod. Phys.* **2011**, *83*, 1057−1110.
(24) Vaziri, S.; Yalon, E.; Rojo, M. M.; Suryavanshi, S. V.; Zhang, H.; McClellan, C. J.; Bailey, C. S.; Smithe, K. K. H.; Gabourie, A. J.; Chen, V.; et al. Ultrahigh thermal isolation across heterogeneously layered two-dimensional materials. *Sci. Adv.* **2019**, *5*, No. eaax1325.
(25) Hicks, L. D.; Dresselhaus, M. S. Effect of quantum-well structures on the thermoelectric figure of merit. *Phys. Rev. B* **1993**, *47*, 12727.
(26) Heremans, J. P.; Dresselhaus, M. S.; Bell, L. E.; Morelli, D. T. When thermoelectrics reached the nanoscale. *Nat. Nanotechnol.* **2013**, *8*, 471−473.
(27) Mahan, G. D.; Sofo, J. O. The best thermoelectric. *Proc. Natl. Acad. Sci. U.S.A.* **1996**, *93*, 7436−7439.
(28) Pei, Y.; Shi, X.; LaLonde, A.; Wang, H.; Chen, L.; Snyder, G. J. Convergence of electronic bands for high performance bulk thermoelectrics. *Nature* **2011**, *473*, 66−69.
(29) Parker, D.; Chen, X.; Singh, D. J. High three-dimensional thermoelectric performance from low-dimensional bands. *Phys. Rev. Lett.* **2013**, *110*, No. 146601.
(30) Bilc, D. I.; Hautier, G.; Waroquiers, D.; Rignanese, G.-M.; Ghosez, P. Low-dimensional transport and large thermoelectric power factors in bulk semiconductors by band engineering of highly directional electronic states. *Phys. Rev. Lett.* **2015**, *114*, No. 136601.
(31) Lee, M.-J.; Ahn, J.-H.; Sung, J. H.; Heo, H.; Jeon, S. G.; Lee, W.; Song, J. Y.; Hong, K.-H.; Choi, B.; Lee, S.-H.; et al. Thermoelectric materials by using two-dimensional materials with negative correlation between electrical and thermal conductivity. *Nat. Commun.* **2016**, *7*, No. 12011.
(32) Zeng, Z.; Sun, X.; Zhang, D.; Zheng, W.; Fan, X.; He, M.; Xu, T.; Sun, L.; Wang, X.; Pan, A. Controlled vapor growth and nonlinear optical applications of large-area 3R phase WS_2 and WSe_2 atomic layers. *Adv. Funct. Mater.* **2019**, *29*, No. 1806874.
(33) Yumnam, G.; Pandey, T.; Singh, A. K. High temperature thermoelectric properties of Zr and Hf based transition metal dichalcogenides: a first principles study. *J. Chem. Phys.* **2015**, *143*, No. 234704.
(34) Glebko, N.; Aleksandrova, I.; Tewari, G. C.; Tripathi, T. S.; Karppinen, M.; Karttunen, A. J. Electronic and vibrational properties of TiS_2, ZrS_2, and HfS_2: periodic trends studied by dispersion-corrected hybrid density functional methods. *J. Phys. Chem. C* **2018**, *122*, 26835−26844.
(35) Li, J.; Shen, J.; Ma, Z.; Wu, K. Thickness-controlled electronic structure and thermoelectric performance of ultrathin SnS_2 nanosheets. *Sci. Rep.* **2017**, *7*, No. 8914.
(36) Sun, B.-Z.; Ma, Z.; Hea, C.; Wu, K. Anisotropic thermoelectric properties of layered compounds in SnX_2 (X = S, Se): a promising thermoelectric material. *Phys. Chem. Chem. Phys.* **2015**, *17*, 29844−29853.
(37) Ding, Y.; Xiao, B.; Tang, G.; Hong, J. Transport properties and high thermopower of $SnSe_2$: a full ab-initio investigation. *J. Phys. Chem. C* **2017**, *121*, 225−236.
(38) Zhang, G.; Zhang, Y.-W. Thermoelectric properties of two-dimensional transition metal dichalcogenides. *J. Mater. Chem. C* **2017**, *5*, 7684−7698.
(39) Ghosh, K.; Singisetti, U. Thermoelectric transport coefficients in mono-layer MoS_2 and WSe_2: role of substrate, interface phonons, plasmon, and dynamic screening. *J. Appl. Phys.* **2015**, *118*, No. 135711.
(40) Wickramaratne, D.; Zahid, F.; Lake, R. K. Electronic and thermoelectric properties of few-layer transition metal dichalcogenides. *J. Chem. Phys.* **2014**, *140*, No. 124710.
(41) Chen, K.-X.; Wang, X.-M.; Mo, D.-C.; Lyu, S.-S. Thermoelectric properties of transition metal dichalcogenides: from monolayers to nanotubes. *J. Phys. Chem. C* **2015**, *119*, 26706−26711.
(42) Özbal, G.; Senger, R. T.; Sevik, C.; Sevinçli, H. Ballistic thermoelectric properties of monolayer semiconducting transition metal dichalcogenides and oxides. *Phys. Rev. B* **2019**, *100*, No. 085415.
(43) Singh, D.; Ahuja, R. Enhanced optoelectronic and thermoelectric properties by intrinsic structural defects in monolayer HfS_2. *ACS Appl. Energy Mater.* **2019**, *2*, 6891−6903.
(44) Gonzalez, J. M.; Oleynik, I. I. Layer-dependent properties of SnS_2 and $SnSe_2$ two-dimensional materials. *Phys. Rev. B* **2016**, *94*, No. 125443.
(45) Roldán, R.; Silva-Guillén, J. A.; López-Sancho, M. P.; Guinea, F.; Cappelluti, E.; Ordejón, P. Electronic properties of single-layer and multilayer transition metal dichalcogenides MX_2 (M = Mo, W and X = S, Se). *Ann. Phys.* **2014**, *526*, 347−357.
(46) Xia, J.; Yan, J.; Shen, Z. X. Transition metal dichalcogenides: structural, optical and electronic property tuning via thickness and stacking. *FlatChem* **2017**, *4*, 1−19.
(47) Rasmussen, F. A.; Thygesen, K. S. Computational 2D materials database: electronic structure of transition-metal dichalcogenides and oxides. *J. Phys. Chem. C* **2015**, *119*, 13169−13183.
(48) Maniadaki, A. E.; Kopidakis, G.; Remediakis, I. N. Strain engineering of electronic properties of transition metal dichalcogenide monolayers. *Solid State Commun.* **2016**, *227*, 33−39.
(49) Johari, P.; Shenoy, V. B. Tuning the electronic properties of semiconducting transition metal dichalcogenides by applying mechanical strains. *ACS Nano* **2012**, *6*, 5449−5456.
(50) Bilc, D. I.; Orlando, R.; Shaltaf, R.; Rignanese, G.-M.; Iniguez, J.; Ghosez, P. Hybrid exchange-correlation functional for accurate prediction of the electronic and structural properties of ferroelectric oxides. *Phys. Rev. B* **2008**, *77*, No. 165107.
(51) Goffinet, M.; Hermet, P.; Bilc, D. I.; Ghosez, P. Hybrid functional study of prototypical multiferroic bismuth ferrite. *Phys. Rev. B* **2009**, *79*, No. 014403.
(52) Prikockytė, A.; Bilc, D.; Hermet, P.; Dubourdieu, C.; Ghosez, P. First-principles calculations of the structural and dynamical properties of ferroelectric $YMnO_3$. *Phys. Rev. B* **2011**, *84*, No. 214301.
(53) Dovesi, R.; Erba, A.; Orlando, R.; Zicovich-Wilson, C. M.; Civalleri, B.; Maschio, L.; Rerat, M.; Casassa, S.; Baima, J.; Salustro, S.; et al. Quantum-mechanical condensed matter simulations with CRYSTAL. *WIREs Comput. Mol. Sci.* **2018**, *8*, No. e1360.
(54) Valenzano, L.; Civalleri, B.; Chavan, S.; Bordiga, S.; Nilsen, M.; Jakobsen, S.; Lillerud, K. P.; Lamberti, C. Disclosing the complex structure of UiO-66 MOF: a synergic combination of experiment and theory. *Chem. Mater.* **2011**, *23*, 1700−1718.
(55) Bredow, T.; Heitjans, P.; Wilkening, M. Electric field gradient calculations for Li_xTiS_2 anci-7 NMR results. *Phys. Rev. B* **2004**, *70*, No. 115111.
(56) Vilela Oliveira, D.; Peintinger, M. F.; Laun, J.; Bredow, T. BSSE-correction scheme for consistent gaussian basis sets of double- and triple-zeta valence with polarization quality for solid-state calculations. *J. Comput. Chem.* **2019**, *40*, 2364−2376.
(57) Laun, J.; Oliveira, D. V.; Bredow, T. Consistent gaussian basis sets of double- and triple-zeta valence with polarization quality of the fifth period for solid-state calculations. *J. Comput. Chem.* **2018**, *39*, 1285−1290.
(58) Pike, N. A.; Dewandre, A.; Troeye, B. V.; Gonze, X.; Verstraete, M. J. Vibrational and dielectric properties of the bulk transition metal dichalcogenides. *Phys. Rev. Mater.* **2018**, *2*, No. 063608.
(59) Blaha, P.; Schwarz, K.; Tran, F.; Laskowski, R.; Madsen, G. K. H.; Marks, L. D. WIEN2k: an APW+lo program for calculating the properties of solids. *J. Chem. Phys.* **2020**, *152*, No. 074101.

https://doi.org/10.1021/acs.jpcc.1c07088
J. Phys. Chem. C XXXX, XXX, XXX−XXX

(60) Corà, F.; Patel, A.; Harrison, N. M.; Dovesi, R.; Catlow, C. R. A. An ab-initio Hartree-Fock study of the cubic and tetragonal phases of bulk tungsten trioxide. *J. Am. Chem. Soc.* **1996**, *118*, 12174−12182.
(61) Muñoz-Ramo, D.; Gavartin, J. L.; Shluger, A. L.; Bersuker, G. Spectroscopic properties of oxygen vacancies in monoclinic HfO_2 calculated with periodic and embedded cluster density functional theory. *Phys. Rev. B* **2007**, *75*, No. 205336.
(62) Madsen, G. K. H.; Singh, D. J. BoltzTraP. A code for calculating band-structure dependent quantities. *Comput. Phys. Commun.* **2006**, *175*, 67−71.
(63) Hosseini, M.; Elahi, M.; Pourfath, M.; Esseni, D. Strain-induced modulation of electron mobility in single-layer transition metal dichalcogenides MX_2 (M=Mo, W; X=S, Se). *IEEE Trans. Electron Devices* **2015**, *62*, 3192−3198.
(64) Sohier, T.; Campi, D.; Marzari, N.; Gibertini, M. Mobility of two-dimensional materials from first principles in an accurate and automated framework. *Phys. Rev. Mater.* **2018**, *2*, No. 114010.
(65) Jalil, O.; Ahmad, S.; Liu, X.; Ang, K. W.; Younis, U. Towards theoretical framework for probing the accuracy limit of electronic transport properties of $SnSe_2$ using many-body calculations. *Europhys. Lett.* **2020**, *130*, No. 57001.
(66) Perdew, J. P.; Burke, K.; Ernzerhof, M. Generalized gradient approximation made simple. *Phys. Rev. Lett.* **1996**, *77*, No. 3865.
(67) Grimme, S.; Antony, J.; Ehrlich, S.; Krieg, H. A consistent and accurate ab initio parametrization of density functional dispersion correction (DFT-D) for the 94 elements H-Pu. *J. Chem. Phys.* **2010**, *132*, No. 154104.
(68) Li, W.; Walther, C. F. J.; Kuc, A.; Heine, T. Density functional theory and beyond for band-gap screening: performance for transition-metal oxides and dichalcogenides. *J. Chem. Theory Comput.* **2013**, *9*, 2950−2958.
(69) Glebko, N.; Aleksandrova, I.; Tewari, G. C.; Tripathi, T. S.; Karppinen, M.; Karttunen, A. J. Electronic and vibrational properties of TiS_2, ZrS_2, and HfS_2: periodic trends studied by dispersion-corrected hybrid density functional methods. *J. Phys. Chem. C* **2018**, *122*, 26835−26844.
(70) Zhao, Q.; Guo, Y.; Si, K.; Ren, Z.; Bai, J.; Xu, X. Elastic, electronic, and dielectric properties of bulk and monolayer ZrS_2, $ZrSe_2$, HfS_2, $HfSe_2$ from van der Waals density-functional theory. *Phys. Status Solidi B* **2017**, *254*, No. 1700033.
(71) Jiang, H. Electronic band structures of molybdenum and tungsten dichalcogenides by the GW approach. *J. Phys. Chem. C* **2012**, *116*, 7664−7671.
(72) Jiang, H. Structural and electronic properties of ZrX_2 and HfX_2 (X = S and Se) from first principles calculations. *J. Chem. Phys.* **2011**, *134*, No. 204705.
(73) Gusakova, J.; Wang, X.; Shiau, L. L.; Krivosheeva, A.; Shaposhnikov, V.; Borisenko, V.; Gusakov, V.; Tay, B. K. Electronic properties of bulk and monolayer TMDs: theoretical study within DFT framework (GVJ-2e method). *Phys. Status Solidi A* **2017**, *214*, No. 1700218.
(74) Bastos, C. M. O.; Besse, R.; Da Silva, J. L. F.; Sipahi, G. M. Ab initio investigation of structural stability and exfoliation energies in transition metal dichalcogenides based on Ti-, V-, and Mo-group elements. *Phys. Rev. Mater.* **2019**, *3*, No. 044002.
(75) Gonzalez, J. M.; Oleynik, I. I. Layer-dependent properties of SnS_2 and $SnSe_2$ two-dimensional materials. *Phys. Rev. B* **2016**, *94*, No. 125443.
(76) Villars, P.; Calvert, L. D. *Pearson's Handbook of Crystallographic Data for Intermetallic Phases*; American Society for Metals International: Materials Park, OH, 1991.
(77) Kam, K. K.; Parkinson, B. A. Detailed photocurrent spectroscopy of the semiconducting group VIB transition metal dichalcogenides. *J. Phys. Chem. A.* **1982**, *86*, 463−467.
(78) Böker, T.; Severin, R.; Müller, A.; Janowitz, C.; Manzke, R.; Voß, D.; Krüger, P.; Mazur, A.; Pollmann, J. Band structure of MoS_2, $MoSe_2$, and α-$MoTe_2$: angle-resolved photoelectron spectroscopy and ab initio calculations. *Phys. Rev. B* **2001**, *64*, No. 235305.
(79) Mak, K. F.; Lee, C.; Hone, J.; Shan, J.; Heinz, T. F. Atomically thin MoS_2: a new direct-gap semiconductor. *Phys. Rev. Lett.* **2010**, *105*, No. 136805.
(80) Zeng, H.; Liu, G.-B.; Dai, J.; Yan, Y.; Zhu, B.; He, R.; Xie, L.; Xu, S.; Chen, X.; Yao, W.; et al. Optical signature of symmetry variations and spin-valley coupling in atomically thin tungsten dichalcogenides. *Sci. Rep.* **2013**, *3*, No. 1608.
(81) Lezama, I. G.; Ubaldini, A.; Longobardi, M.; Giannini, E.; Renner, C.; Kuzmenko, A. B.; Morpurgo, A. F. Surface transport and band gap structure of exfoliated 2H-$MoTe_2$ crystals. *2D Mater.* **2014**, *1*, No. 021002.
(82) Greenaway, D. L.; Nitsche, R. Preparation and optical properties of group IV-VI_2 chalcogenides having the CdI_2 structure. *J. Phys. Chem. Solids* **1965**, *26*, 1445−1458.
(83) Lee, P. A.; Said, G.; Davis, R.; Lim, T. H. On the optical properties of some layer compounds. *J. Phys. Chem. Solids* **1969**, *30*, 2719−2729.
(84) Roubi, L.; Carlone, C. Resonance Raman spectrum of HfS_2 and ZrS_2. *Phys. Rev. B* **1988**, *37*, 6808.
(85) Terashima, K.; Imai, I. Indirect absorption edge of ZrS_2 and HfS_2. *Solid State Commun.* **1987**, *63*, 315−318.
(86) Starnberg, H. I.; Brauer, H. E.; Hughes, H. P. Photoemission studies of the conduction band filling in $Ti_{1.05}S_2$ and Cs-intercalated TiS_2 and $ZrSe_2$. *J. Phys.: Condens. Matter* **1996**, *8*, 1229−1234.
(87) Domingo, G.; Itoga, R. S.; Kannewurf, C. R. Fundamental optical absorption in SnS_2 and $SnSe_2$. *Phys. Rev.* **1966**, *143*, No. 536.
(88) Burton, L. A.; Whittles, T. J.; Hesp, D.; Linhart, W. M.; Skelton, J. M.; Hou, B.; Webster, R. F.; O'Dowd, G.; Reece, C.; Cherns, D.; et al. Electronic and optical properties of single crystal SnS_2: an earth-abundant disulfide photocatalyst. *J. Mater. Chem. A* **2016**, *4*, 1312−1318.
(89) Manou, P.; Kalomiros, J. A.; Anagnostopoulos, A. N.; Kambas, K. Optical properties of $SnSe_2$ single crystals. *Mater. Res. Bull.* **1996**, *31*, 1407−1415.
(90) Kuc, A.; Heine, T. The electronic structure calculations of two-dimensional transition-metal dichalcogenides in the presence of external electric and magnetic fields. *Chem. Soc. Rev.* **2015**, *44*, 2603−2614.
(91) Steinberg, S.; Dronskowski, R. The crystal orbital Hamilton population (COHP) method as a tool to visualize and analyze chemical bonding in intermetallic compounds. *Crystals* **2018**, *8*, No. 225.
(92) Yokoi, H.; Takeyama, S.; Miura, N.; Bauer, G. Anomalous temperature dependence of the effective mass in n-type PbTe. *Phys. Rev. B* **1991**, *44*, No. 6519.
(93) Bilc, D. I.; Mahanti, S. D.; Kanatzidis, M. G. Electronic transport properties of PbTe and $AgPb_mSbTe_{2+m}$ systems. *Phys. Rev. B* **2006**, *74*, No. 125202.
(94) Köhler, H. Non-parabolic E(k) relation of the lowest conduction band in Bi_2Te_3. *Phys. Status Solidi B* **1976**, *73*, 95−104.
(95) Jacquot, A.; Farag, N.; Jaegle, M.; Bobeth, M.; Schmidt, J.; Ebling, D.; Bottner, H. Thermoelectric properties as a function of electronic band structure and microstructure of textured materials. *J. Electron. Mater.* **2010**, *39*, 1861−1868.
(96) Julien, C.; Eddrief, M.; Samaras, I.; Balkanski, M. Optical and electrical characterizations of SnSe, SnS_2 and $SnSe_2$ single crystals. *Mater. Sci. Eng., B* **1992**, *15*, 70−72.
(97) El-Mahalawy, S. H.; Evans, B. L. Temperature dependence of the electrical conductivity and Hall coefficient in 2H-MoS_2, $MoSe_2$, WSe_2, and $MoTe_2$. *Phys. Status Solidi B* **1977**, *79*, 713−722.
(98) Pisoni, A.; Jacimovic, J.; Barišić, O. S.; Walter, A.; Náfrádi, B.; Bugnon, P.; Magrez, A.; Berger, H.; Revay, Z.; Forró, L. The role of transport agents in MoS_2 single crystals. *J. Phys. Chem. C* **2015**, *119*, 3918−3922.
(99) Yoshida, M.; Iizuka, T.; Saito, Y.; Onga, M.; Suzuki, R.; Zhang, Y.; Iwasa, Y.; Shimizu, S. Gate-optimized thermoelectric power factor in ultrathin WSe_2 single crystals. *Nano Lett.* **2016**, *16*, 2061−2065.

https://doi.org/10.1021/acs.jpcc.1c07088
J. Phys. Chem. C XXXX, XXX, XXX−XXX

(100) McKinney, R.; Gorai, P.; Toberer, E. S.; Stevanovic, V. Rapid prediction of anisotropic lattice thermal conductivity: application to layered materials. *Chem. Mater.* **2019**, *31*, 2048−2057.
(101) Busch, G.; Froehlich, C.; Hulliger, F.; Steigmeier, E. Structure, electrical, and thermoelectric properties of $SnSe_2$. *Helv. Phys. Acta* **1961**, *34*, 359−368.
(102) Ding, Y.; Xiao, B.; Tang, G.; Hong, J. Transport properties and high thermopower of $SnSe_2$: a full ab-initio investigation. *J. Phys. Chem. C* **2017**, *121*, 225−236.
(103) Zhou, C.; Yu, Y.; Zhang, X.; Cheng, Y.; Xu, J.; Lee, Y. K.; Yoo, B.; Cojocaru-Mirédin, O.; Liu, G.; Cho, S.-P.; et al. Cu intercalation and Br doping to thermoelectric $SnSe_2$ lead to ultrahigh electron mobility and temperature-independent power factor. *Adv. Funct. Mater.* **2020**, *30*, No. 1908405.
(104) Luo, Y.; Zheng, Y.; Luo, Z.; Hao, S.; Du, C.; Liang, Q.; Li, Z.; Khor, K. A.; Hippalgaonkar, K.; Xu, J.; et al. n-Type $SnSe_2$ oriented-nanoplate-based pellets for high thermoelectric performance. *Adv. Energy Mater.* **2018**, *8*, No. 1702167.
(105) Li, F.; Zheng, Z.; Li, Y.; Wang, W.; Li, J.-F.; Li, B.; Zhong, A.; Luo, J.; Fan, P. Ag-doped $SnSe_2$ as a promising mid-temperature thermoelectric material. *J. Mater. Sci.* **2017**, *52*, 10506−10516.
(106) Yakovleva, G. E.; Romanenko, A. I.; Ledneva, A. Y.; Belyavin, V. A.; Kuznetsov, V. A.; Berdinsky, A. S.; Burkov, A. T.; Konstantinov, P. P.; Novikov, S. V.; Han, M.-K.; et al. Thermoelectric properties of $W_{1-x}Nb_xSe_{2-y}S_y$ polycrystalline compounds. *J. Am. Ceram. Soc.* **2019**, *102*, 6060−6067.
(107) Choe, J. S.; Lee, C.; Kim, M. J.; Lee, G.-G.; Shim, J.-H.; Lim, Y. S. Bader net charge analysis on doping effects of Sb in $SnSe_2$ and related charge transport properties. *J. Appl. Phys.* **2020**, *127*, No. 185706.
(108) Vaney, J.-B.; Yamini, S. A.; Takaki, H.; Kobayashi, K.; Kobayashi, N.; Mori, T. Magnetism-mediated thermoelectric performance of the Cr-doped bismuth telluride tetradymite. *Mater. Today Phys.* **2019**, *9*, No. 100090.
(109) Sun, P.; Kumar, K. R.; Lyu, M.; Wang, Z.; Xiang, J.; Zhang, W. Generic Seebeck effect from spin entropy. *Innovation* **2021**, *2*, No. 100101.
(110) Slade, T. J.; Grovogui, J. A.; Kuo, J. J.; Anand, S.; Bailey, T. P.; Wood, M.; Uher, C.; Snyder, G. J.; Dravid, V. P.; Kanatzidis, M. G. Understanding the thermally activated charge transport in $NaPb_mSbQ_{m+2}$ (Q = S, Se, Te) thermoelectrics: weak dielectric screening leads to grain boundary dominated charge carrier scattering. *Energy Environ. Sci.* **2020**, *13*, 1509−1518.

https://doi.org/10.1021/acs.jpcc.1c07088
J. Phys. Chem. C XXXX, XXX, XXX−XXX